Editors' Suggestion

Valley Two-Qubit System in a MoS_2-Monolayer Gated Double Quantum dot

J. Pawłowski,[1,*] M. Bieniek,[1,2] and T. Woźniak[3]

[1] *Department of Theoretical Physics, Wrocław University of Science and Technology, Wybrzeże Wyspiańskiego 27, 50-370 Wrocław, Poland*

[2] *Department of Physics, University of Ottawa, Ottawa, Ontario K1N 6N5, Canada*

[3] *Department of Semiconductor Materials Engineering, Wrocław University of Science and Technology, Wybrzeże Wyspiańskiego 27, 50-370 Wrocław, Poland*

(Received 24 February 2021; accepted 15 April 2021; published 12 May 2021)

We explore a two-qubit system defined on valley isospins of two electrons confined in a gate-defined double quantum dot created within a MoS_2 monolayer flake. We show how to initialize, control, interact, and read out such valley qubits by only electrical means using voltages applied to the local planar gates, which are layered on the top of the flake. By demonstrating the two-qubit exchange or readout via the Pauli blockade, we prove that valley qubits in the transition-metal-dichalcogenide semiconductor family fulfill the universality criteria and represent a scalable quantum-computing platform. Our numerical experiments are based on the tight-binding model for a MoS_2 monolayer, which gives single-electron eigenstates that are then used to construct a basis of Slater determinants for the two-electron configuration space. We express screened electron-electron interactions in this basis by calculating the Coulomb matrix elements using localized Slater-type orbitals. Then we solve the time-dependent Schrödinger equation and obtain an exact time evolution of the two-electron system. During the evolution we simultaneously solve the Poison equation, finding the confinement potential controlled via voltages applied to the gates.

DOI: 10.1103/PhysRevApplied.15.054025

I. INTRODUCTION

In recent years quantum computing has experienced a return of great interest mainly due to advances in scaling multiqubit registers into devices composed of dozens of qubits, such as the Google superconducting quantum computer [1,2], in the case of which authors claim to have achieved quantum supremacy [3]. However, the road to realizing systems that scale to hundreds of logical qubits (each of them storing dozens of noisy qubits with applied quantum error-correction codes [4]) is still a long way off, and intensive work is currently applied to other approaches to implement qubits in a solid-state quantum computer [5–12].

Two-dimensional (2D) crystals consisting of single layers of atoms are modern materials that can be used to implement quantum computations. Two-dimensional monolayers of transition-metal dichalcogenides (TMDCs) (e.g., MoS_2) seem to be better candidates than graphene because they have wide direct band gaps and strong spin-orbit coupling [13,14]. The spin-orbit coupling allows one to perform quantum operations on a qubit defined on the spin of a confined electron. However, TMDC monolayers have no inversion centers to allow access to an extra degree of freedom of charge carriers, the so-called $\mathcal{K}$-valley index, which opens up an intriguing prospect to define a valley-based qubit [15–17] or to create a spin-valley two-qubit system [18–20].

A valley-based information carrier is also postulated in many other materials and arrangements. It was explored in carbon nanotubes [21,22], TMDCs [23,24], and graphene bilayers [25], and very recently a fast valley qubit in silicon was proposed [26,27]. Deformations of the structure of a graphene flake induce pseudo-magnetic-fields that couple the K and K' valleys with opposite signs [28], resulting in the valley splitting or the generation of valley polarization, thus working as a *valleytronic* filtering device [29,30]. Also, the electrically controlled valley degree of freedom was reported in twisted WS_2 bilayers [31]. TMDC monolayers are attractive also from the point of view of optical manipulation of valleys [32–37], which has been widely used to study initialization and coherence of this degree of freedom [38–42], also including interesting many-body effects related to valley polarization [43–45]. The excess electron gas in these systems [46–51] potentially provides additional means of control as recently examined experimentally [52,53]. In this work, however, we focus on all-electrical manipulation protocols due to their potentially improved scalability in large multiqubit systems.

*jaroslaw.pawlowski@pwr.edu.pl

It is known that for carriers that are spatially localized, the valley degree of freedom is still well defined. There are many theoretical [13,16,17,54–64] and experimental [52,65–69] studies of quantum dots (QDs) based on MoS_2 and related TMDCs pointing toward promising routes to various spin-valley massive-Dirac-fermion-based qubit realizations, as summarized recently in Ref. [70]. We also note that the rich physics of single-body [71,72] and many-body [73] properties of such dots, combined with tunability via heterostructure details or proper substrate engineering, may lead to even greater interest in these systems. Also, experimental demonstrations of TMDC-based QDs are still in an early phase, and significant progress in this direction is expected in the coming years.

In our recent work [17] we proposed a valley-qubit implementation and proved that it is possible to perform single valley-qubit operations in monolayer TMDCs. Here we extend this idea to two-electron systems. We achieve this by using a pair of qubits and coupling them in a controlled manner to perform two-qubit operations. For this we propose a nanodevice based on a gate-defined [74] double QD [75–78] within a MoS_2 monolayer in which we confine two electrons. Using quantum-computing language, we identify two-qubit states of the two-electron system as described by the left-dot (L) and right-dot (R) valley index (showing which valley, i.e., K or K', is occupied) for a chosen spin orientation (e.g., spin-up, $\uparrow$). This means that single qubit state is pinned to the specific dot, not to the electron, which is delocalized between the dots. In our proposal the two-qubit $|00\rangle$ state is associated with $|K'_{\uparrow,L}K'_{\uparrow,R}\rangle$, where L and R indicate the left dot and the right dot, respectively. The remaining two-qubit basis states are defined as $|01\rangle = |K'_{\uparrow,L}K_{\uparrow,R}\rangle$, $|10\rangle = |K_{\uparrow,L}K'_{\uparrow,R}\rangle$, and $|11\rangle = |K_{\uparrow,L}K_{\uparrow,R}\rangle$. For brevity, in the next sections we drop the L and R indices. By applying control voltages to the gates, we modulate the confinement potential, forcing in this way intervalley transitions [55] of each qubit associated with each dot, and adjust the potential barrier between them. Accurate modeling of the Coulomb interaction enables us to correctly describe the valley-swap operation between qubits, as well as the qubit initialization and readout via the valley Pauli blockade [22,79].

This paper is organized as follows: In Sec. II we propose and describe a realistic nanodevice structure. In Sec. III we discuss the theoretical tools used (i.e., single-electron and two-electron theory), details for calculating the Coulomb integrals, the electrostatic potential model, and the time-dependent simulations. Readers interested in the results may omit Sec. III and proceed to Sec. IV, in which states of the double QD are discussed. Then, in Secs. V and VI, results for the electrically driven valley exchange and the valley-Pauli-blockade readout mechanism are discussed. We conclude with a summary in Sec. VII.

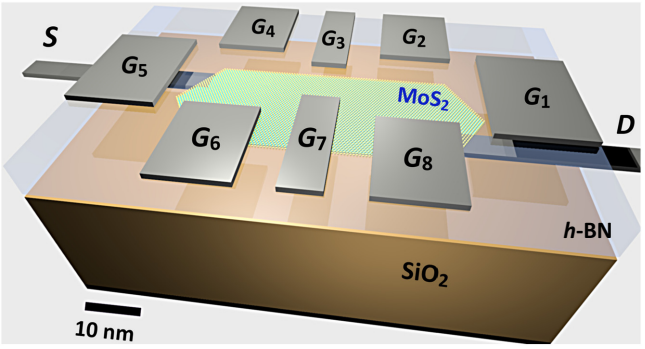

FIG. 1. Structure of the proposed device consisting of a MoS_2 nanoflake with nearby source (S) and drain (D) electrodes deposited on a SiO_2 layer placed on a highly doped substrate serving as the back gate, together with the layout of eight gates (G_1–G_8) separated from the flake by a h-BN barrier layer.

II. DEVICE STRUCTURE

The structure of the proposed nanodevice is presented in Fig. 1. On a strongly doped silicon substrate (Si^{n++}) we place a 25-nm-thick layer of SiO_2. Then we place two electrodes that serve as a source (S) and a drain (D) and deposit a MoS_2-monolayer ribbon of the shape and dimensions presented in Fig. 2. The monolayer is then covered with a 5-nm-thick insulating layer of hexagonal boron nitride (h-BN), which has a large band gap [80], forming a tunnel barrier. Finally, on top of this layered structure, we lay down eight control gates G_1–G_8, as presented in Fig. 1. Three of them, 15-nm-wide G_1 and 10-nm-wide pair of G_2 and G_8, are placed around the right-dot region and form its confinement. Similarly, 15-nm-wide G_5 and the 10-nm-wide pair of G_4 and G_6 form the left dot. Left and right dots are separated by a controllable barrier generated by a pair of elongated gates, G_3 and G_7. The structure of the proposed device is very similar to the one described in Ref. [69], albeit with a reversed ordering of layers (i.e., in our case the role of the top gate is taken over by the strongly doped substrate).

The gate layout presented enables us to create a confinement potential forming a double-QD structure within the flake. With the tunable barrier height between the dots (controlled via G_3 and G_7) and variable locations of the dot-potential minima (via G_1, G_2, and G_8 or via G_4, G_5, and G_6) and confinement depth (by tuning the negative bias voltage applied to all gates), we can efficiently control each dot confinement, as well as the potential offset between the dots (via G_1 and G_5). The potential $\phi(\mathbf{r})$ in the entire nanodevice, controlled by the gate voltages, is calculated by solving the generalized Poisson's equation [81], while the electron states in the flake are described with the tight-binding (TB) formalism.

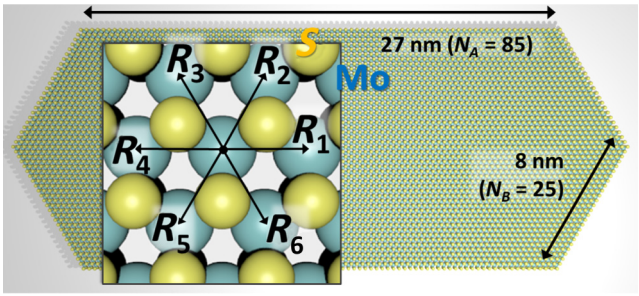

FIG. 2. The MoS_2 monolayer flake used in the device has an elongated hexagonal shape with sides made of $N_A = 85$ or $N_B = 25$ Mo atoms, making the bottom side 27 nm long and the lateral sides 8 nm long (the distance between Mo nodes is 0.319 nm). The inset shows the structure of the MoS_2 crystal lattice formed of hexagonally packed Mo and S atoms arranged in triangular lattices rotated relative to each other by π. The Mo lattice vectors R_p determine the hopping directions in our nearest-neighbor TB model.

III. MODEL AND METHODS

A. Single-electron tight-binding theory

The flake used in our device is a monolayer made of molybdenum disulfide. This semiconductor is successfully described by several TB models with various numbers of orbitals used [82–84], although, at least six Mo and S orbitals [82] with next-nearest-neighbor hoppings are necessary to construct a minimal TB model that reproduces the low-energy physics around the Fermi level in the entire Brillouin zone. It has been shown that a simple three-Mo-orbital TB model [85] on a triangular lattice can correctly represent the dispersion relation and the orbital composition close to the K point in the Brillouin zone near the band edges, where the Bloch states consist mainly of Mo d orbitals [86]. Because in our calculations we are concerned solely with states derived from the minimum in the conduction band (CB) at $\pm K$ points, we can safely ignore the multivalley structure of the conduction band [72,82] and focus on a simple, effective description of the confined electron states. Consequently, we describe the monolayer structure using three Mo orbitals, d_{z^2}, d_{xy}, and $d_{x^2-y^2}$, with the nearest-neighbor hoppings [85]:

$$H_{1e} = \sum_{m\sigma\sigma'\alpha\beta} \left[\delta_{\sigma\sigma'}\delta_{\alpha\beta}(\epsilon_\alpha + \varphi_m)\,\hat{n}_{m\alpha\sigma} + s^z_{\sigma\sigma'}\lambda_{\alpha\beta}\,\hat{c}^\dagger_{m\alpha\sigma}\hat{c}_{m\beta\sigma'}\right] + \sum_{\langle mn\rangle\,\sigma\sigma'\alpha\beta} \delta_{\sigma\sigma'}t^{\langle mn\rangle}_{\alpha\beta}\,\hat{c}^\dagger_{m\alpha\sigma}\hat{c}_{n\beta\sigma} + H_Z. \quad (1)$$

Indices $\{m,n\}$, $\{\sigma,\sigma'\}$, and $\{\alpha,\beta\}$ enumerate lattice sites, spins, and orbitals; for example, the operator $\hat{c}^\dagger_{m\alpha\sigma}$ ($\hat{c}_{m\alpha\sigma}$) creates (annihilates) an electron with orbital α and spin σ at the mth lattice site. Also, we abbreviate $\hat{n} = \hat{c}^\dagger\hat{c}$. On-site energies for orbitals α are parametrized by ϵ_α. The potential energy of the electrostatic confinement at the mth lattice site $\varphi_m = -|e|\phi(x_m, y_m)$ together with the on-site energies ϵ_α enters the diagonal matrix elements. $\lambda_{\alpha\beta}$ expresses the intrinsic spin-orbit coupling [14], s_z stands for the z-Pauli-matrix, and H_Z stands for the Zeeman Hamiltonian, which is added whenever the response to a magnetic field is studied.

The off-diagonal electron-hopping element from the β Mo orbital localized in the nth lattice site to the α orbital localized in the mth site is denoted by $t^{\langle mn\rangle}_{\alpha\beta} \equiv t_{\alpha\beta}\big(R_{p(m,n)}\big)$. We note that it does not flip spin, as explicitly written with Kronecker delta $\delta_{\sigma\sigma'}$. It depends on the hopping direction between $\langle m\,n\rangle$ nearest-neighbor pair—that is, it is described by the R_p ($p = 1\cdots 6$) vectors for the Mo lattice; see Fig. 2. They form two nonequivalent families: R_1, R_3, R_5 and R_2, R_4, R_6, which differ by the position of the nearest sulfur (S) neighbor, either on the left side or on the right side. This symmetry constraint is reflected on the reciprocal lattice, where the K points in the corners of the hexagonal Brillouin zone form two nonequivalent families: K and K'. Opposite hoppings are mutually transposed: $t_{\alpha\beta}(R_p) = t_{\beta\alpha}(-R_p)$. Their explicit forms, together with the on-site energies ϵ_α and spin-orbit-coupling parameters $\lambda_{\alpha\beta}$, can be found in Refs. [17,85].

Knowing the tight-binding representation of the flake lattice, we solve the eigenproblem for the single-electron Hamiltonian (1): $H_{1e}\boldsymbol{\psi}_i = \mathcal{E}_i\boldsymbol{\psi}_i$, with eigenenergies $\mathcal{E}_i$. Calculation results are discussed in Sec. IV.

B. Two-electron theory

We use the single-electron eigenstates $\boldsymbol{\psi}_i$ found to construct the two-electron spinor $\langle \mathbf{r}_1\mathbf{r}_2|\tilde{ij}\rangle \equiv \boldsymbol{\Psi}_{ij}(\mathbf{r}_1,\mathbf{r}_2)$ of an antisymmetric form:

$$\boldsymbol{\Psi}_{ij}(\mathbf{r}_1,\mathbf{r}_2) = \frac{1}{\sqrt{2}}\left[\boldsymbol{\psi}_i(\mathbf{r}_1)\otimes\boldsymbol{\psi}_j(\mathbf{r}_2) - \boldsymbol{\psi}_j(\mathbf{r}_1)\otimes\boldsymbol{\psi}_i(\mathbf{r}_2)\right], \quad (2)$$

with spin-orbital notation $\boldsymbol{\psi}_i(\mathbf{r}_a) \equiv [\psi_i^{\sigma\alpha}(\mathbf{r}_a)]$, where $a = 1,2$ (two electrons), $\sigma = 1,2$ (1/2-spin-vector elements), and $\alpha = 1,2,3$ (orbital number). We abbreviate $\boldsymbol{\psi}_i(\mathbf{r}_1)\otimes\boldsymbol{\psi}_j(\mathbf{r}_2) \equiv \langle \mathbf{r}_1\mathbf{r}_2|ij\rangle$, and then $|\tilde{ij}\rangle = (1/\sqrt{2})\,(|ij\rangle - |ji\rangle)$. Taking m single-electron low-energy spin-orbitals near the CB minimum, we combine them into $n = \binom{m}{2}$ two-electron spinors $|\tilde{ij}\rangle$. Next we expand the full two-electron spinor in this basis:

$$\boldsymbol{\Psi}(\mathbf{r}_1,\mathbf{r}_2) = \sum_{k=1}^{n} d_k\,\langle \mathbf{r}_1\mathbf{r}_2|\tilde{ij}\rangle, \quad (3)$$

where $i,j \in \{1,2,\ldots,m\}$, and $n = m(m-1)/2$.

To include electron-electron interactions, the two-electron Hamiltonian is written as

$$H_{2e}(\mathbf{r}_1,\mathbf{r}_2) = H_{1e}(\mathbf{r}_1) + H_{1e}(\mathbf{r}_2) + \bar{V}_C(\mathbf{r}_1,\mathbf{r}_2), \quad (4)$$

where $\bar{V}_C(\mathbf{r}_1,\mathbf{r}_2)=\bar{V}_C(|\mathbf{r}_1-\mathbf{r}_2|)$ is the Coulomb interaction screened by the dielectric environment of the nearby layers, described in detail later.

C. Configuration-interaction method

To describe a two-electron state exactly, we use the configuration-interaction method [87–90], where the Hamiltonian given in Eq. (4) is represented in the two-electron basis [defined in Eq. (3)] of two-particle antisymmetric Slater determinants [given by Eq. (2)], constructed from the single-electron states. In such a basis, with $\langle ij|\bar{V}_C|kl\rangle$ abbreviated as V_{ijkl}, one has [91–93]

$$H_{2e}=\sum_{i<j} d_i^\dagger d_j^\dagger d_i d_j\ \mathcal{E}_{ij}+\sum_{i<j,k<l} d_i^\dagger d_j^\dagger d_k d_l\left(V_{ijkl}-V_{ijlk}\right). \tag{5}$$

Here $d_i^\dagger d_j^\dagger$ creates an electron pair in the $|\tilde{ij}\rangle$ state, and the two-electron energy is defined as $\mathcal{E}_{ij}=\mathcal{E}_i+\mathcal{E}_j$, with $\mathcal{E}_i$ being the energy of a single-electron state $|i\rangle$. An explicit derivation of the Hamiltonian in Eq. (5) can be found in Appendix A. Because of the symmetry constraints, the Coulomb-matrix elements V_{ijkl} obey the following relation:

$$\sum_{i<j,k<l} d_i^\dagger d_j^\dagger d_k d_l\left(V_{ijkl}-V_{ijlk}\right)=\frac{1}{2}\sum_{i,j,k,l} d_i^\dagger d_j^\dagger d_k d_l V_{ijkl}. \tag{6}$$

D. Coulomb integrals

Two-electron scattering-matrix elements $\langle ij|\bar{V}_C|kl\rangle$ are calculated from the two-body localized on-site Coulomb-matrix elements $\langle sp|\bar{V}_C|df\rangle\equiv\mathcal{V}_{spdf}$. To get the latter we expand states $|i\rangle$ in a basis of atomic orbitals η_s^α centered at the lattice nodes $\mathbf{r}_s=(x_s,y_s,0)$. For every two nodes s and p, located in $\mathbf{r}_s$ and $\mathbf{r}_p$, we have $\eta_s^\alpha(\mathbf{r}-\mathbf{r}_s)=\eta_p^\alpha(\mathbf{r}-\mathbf{r}_p)$. On-site states are indexed by indices s, p, d, and f; for example, for s,

$$\langle\mathbf{r}|i\rangle=\boldsymbol{\psi}_i(\mathbf{r})=\sum_{s,\sigma_s,\alpha_s}\psi_{i,s}^{\sigma_s\alpha_s}\eta_s^{\alpha_s}(\mathbf{r}). \tag{7}$$

In some places we abbreviate on-site states as $|s^{\alpha_s}\rangle$; that is, $\eta_s^{\alpha_s}(\mathbf{r})=\langle\mathbf{r}|s^{\alpha_s}\rangle$. We now expand the scattering-matrix elements V_{ijkl} in this new on-site basis of atomic orbitals. We abbreviate $\langle\eta_s^{\alpha_s}\eta_p^{\alpha_p}|\bar{V}_C|\eta_d^{\alpha_d}\eta_f^{\alpha_f}\rangle\equiv\langle s^{\alpha_s}p^{\alpha_p}|\bar{V}_C|d^{\alpha_d}f^{\alpha_f}\rangle\equiv\mathcal{V}_{spdf}^{\alpha_s\alpha_p\alpha_d\alpha_f}$, or simply $\mathcal{V}_{spdf}$. In general we have

$$V_{ijkl}=\sum_{\substack{s,\sigma_s,\alpha_s\\ p,\sigma_p,\alpha_p\\ d,\sigma_d,\alpha_d\\ f,\sigma_f,\alpha_f}}\left(\psi_{i,s}^{\sigma_s\alpha_s}\psi_{j,p}^{\sigma_p\alpha_p}\right)^*\psi_{k,d}^{\sigma_d\alpha_d}\psi_{l,f}^{\sigma_f\alpha_f}\mathcal{V}_{spdf}. \tag{8}$$

In the calculation of V_{ijkl}, the main contribution is from one-center and two-center integrals (i.e., $s=d$ and $p=f$). In addition, the Coulomb interaction does not change spin, and thus $\sigma_s=\sigma_d$ and $\sigma_p=\sigma_f$. Therefore, we can simplify the calculations by taking leading order-of-magnitude elements

$$V_{ijkl}\approx\sum_{\substack{s,\sigma_s,p,\sigma_p\\ \alpha_s\alpha_p,\alpha_d,\alpha_f}}\left(\psi_{i,s}^{\sigma_s\alpha_s}\psi_{j,p}^{\sigma_p\alpha_p}\right)^*\psi_{k,s}^{\sigma_s\alpha_d}\psi_{l,p}^{\sigma_p\alpha_f}\mathcal{V}_{spsp}^{\alpha_s\alpha_p\alpha_d\alpha_f}, \tag{9}$$

with atomic elements defined as

$$\mathcal{V}_{spsp}^{\alpha_s\alpha_p\alpha_d\alpha_f}=\iint d^3r_1 d^3r_2[\eta_s^{\alpha_s}(\mathbf{r}_1)\eta_p^{\alpha_p}(\mathbf{r}_2)]^*\times\eta_s^{\alpha_d}(\mathbf{r}_1)\eta_p^{\alpha_f}(\mathbf{r}_2)\bar{V}_C(\mathbf{r}_1,\mathbf{r}_2). \tag{10}$$

Atomic Coulomb-matrix elements $\mathcal{V}_{spdf}$ are calculated by a Monte Carlo approach with adaptive sampling via the VEGAS algorithm [94]. We assume that localized orbitals $\eta_s^{\alpha_s}(\mathbf{r})$ have a hydrogenlike Slater form [95] with appropriate atomic shielding parameters [91,96]. The molybdenum atomic-shielding constant ζ is in the range between 2.85 and 3.11 (a.u.) [97]. However, because of screening by the sulfur dimers, a smaller ζ value is taken since the actual orbital is slightly widened. We estimate this effect through density-functional-theory (DFT) calculations using the projector-augmented-wave method [98] for atoms and the Perdew-Burke-Ernzerhof parametrization [99] of the generalized-gradient approximation for the exchange-correlation functional, as implemented in VASP [100]. We use a plane-wave-basis cutoff of 400 eV and a $12\times12\times1$ k-point grid. The unit cell contains 15 Å of vacuum in the direction perpendicular to the monolayer. The spin-orbit interaction is taken into account during all calculation steps. This setup ensures consistency with the tight-binding-model parametrization we use from Ref. [85].

In Fig. 3 we plot the electronic charge density for the MoS_2 monolayer along a Mo-Mo line at the CB minimum at the K point obtained from the DFT calculations (blue curve), and compare it with the charge density calculated with Slater-type orbitals $Nr^{n-1}e^{-\zeta r}\,Y_{\mathrm{lm}}$ for molybdenum, which for $4d_{z^2}$ has the form

$$\eta_0^{4d_{z^2}}(r)=\frac{\zeta^{9/2}}{2\sqrt{63\pi}}re^{-\zeta r}(3z^2-r^2), \tag{11}$$

and accounts for 88% of the orbital composition in the CB at the K point. To include the contribution from the Mo atomic core, we add a charge density approximated by a Gaussian fit and shown as the dashed gray curve in Fig. 3. We find that $\zeta=2.9$ (a.u.), taken from the literature, gives a less satisfactory fit to the DFT electron density (green curve) than the tuned value $\zeta=2.45$ (orange), which is assumed when we calculate $\mathcal{V}_{spdf}$, as defined in Eq. (10).

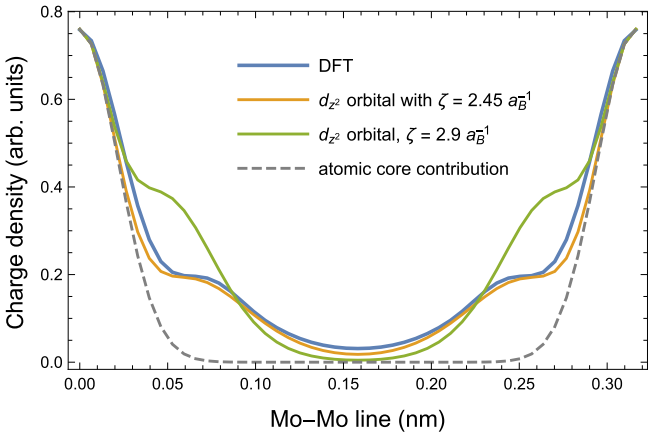

FIG. 3. Fitting of the molybdenum atomic shielding constant ζ. On-site electron density along the Mo-Mo interatomic line in a MoS_2 monolayer calculated within DFT (blue curve) versus the density obtained for the Slater-type orbitals with $\zeta = 2.45a_B^{-1}$ (orange curve) or $\zeta = 2.9a_B^{-1}$ (green curve), together with the assumed atomic core density (dashed gray curve).

During $\mathcal{V}_{spdf}$ calculations, we find that the most-significant contributions come from one-center *direct* integrals [i.e., involving orbitals centered at the same node: $s = p = d = f$ ($3^4 = 81$ different integrals; in practice the number is less due to orbital symmetries)] and two-center integrals: $s = p$ and $d = f$ between the nearest sites [i.e., $\langle 12|\bar{V}_C|12\rangle$ (also 81 elements)]. To simplify the calculations of V_{ijkl} we take the explicit values only for the 75 integrals that are greater than 0.3 eV. They are grouped in Table I in Appendix B, with the largest value reported for each group. The small spread of values within each group of integrals comes from the probabilistic nature of the method used in the calculations. Taking more integrals explicitly (i.e., smaller than the arbitrarily set 0.3-eV threshold) would have no practical impact on the calculations. However, what is important, remaining long-range elements are also taken into account in V_{ijkl}, albeit they are modeled as classical pointlike density-density terms of screened Coulomb interaction $\bar{V}_C(r)$, defined in Appendix C.

The V_{ijkl} elements are calculated once, by summing up $\mathcal{V}_{spdf}$ integrals, as described in Eq. (10), and stored on a hard disk ($80 \times 80 \times 80 \times 79/2$ elements in total) for further use.

E. Electrostatic potential

As discussed previously, the layout of the gates is presented in Fig. 1. The voltages applied to these gates (relative to the substrate) are used to create confinement in the flake. To calculate the realistic electrostatic potential $\phi(\mathbf{r})$ we solve the generalized Poisson equation [81] taking into account voltages V_1–V_8 applied to the control gates

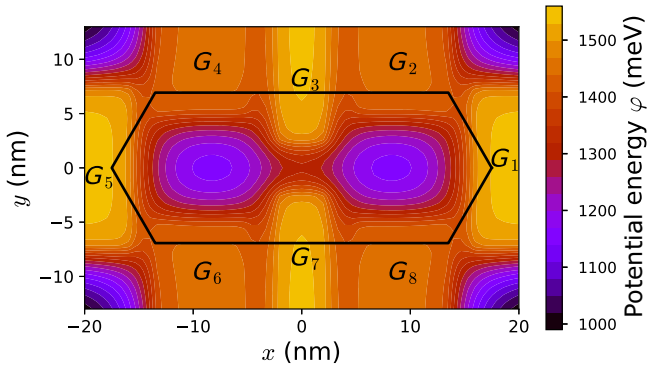

FIG. 4. Confinement potential in the area of the nanoflake (black outline) calculated via the Poisson equation for voltages V_1, V_3, V_5, $V_7 = -1600$ mV and V_2, V_4, V_6, $V_2 = -1500$ mV applied to the nanodevice local gates G_1–G_8 (see Fig. 1). Such gating results in a double-quantum-dot structure created within the nanoflake area.

G_1–G_8 and to the highly doped substrate (kept at the referential potential $V_0 = 0$), together with the space-dependent permittivity of different materials in the device. At the lateral and top sides of the computational box we apply Neumann boundary conditions with a zeroing normal component of the electric field. Further details on the method used can be found in Ref. [17]. The resulting potential in the area between SiO_2 and h-BN layers, where the flake is sandwiched, is presented in Fig. 4, and is calculated for voltages V_1, V_3, V_5, $V_7 = -1600$ mV and V_2, V_4, V_6, $V_8 = -1500$ mV applied to the local gates. At the same time, voltage $V_B = -1600$ mV applied to gates G_3 and G_7 controls the height of the interdot barrier.

F. Time-dependent simulations

We have learned how to calculate eigenstates of a two-electron system confined within a double quantum dot with an included Coulomb interaction. Such dressed states, each described by a set of $m(m-1)/2$ ($m = 80$) d_{ij} amplitudes, serve as initial states for the time-dependent simulations that we introduce now.

To control qubits we apply time-varying voltages to the device gates. Evolution of the system wave function induced in this way is described within our configuration-interaction basis, albeit now with time-dependent amplitudes $d_{ij}(t)$, constituting the time-dependent configuration-interaction method. Insertion of $\Psi(\mathbf{r}_1, \mathbf{r}_2, t) = \sum_{i<j} d_{ij}(t)\ \Psi_{ij}(\mathbf{r}_1, \mathbf{r}_2) e^{-(i/\hbar)\mathcal{E}_{ij}t}$ into the Schrödinger equation with the time-dependent Hamiltonian

$$H_{2e}(\mathbf{r}_1, \mathbf{r}_2, t) = H_{2e}(\mathbf{r}_1, \mathbf{r}_2) + \delta\varphi(\mathbf{r}_1, t) + \delta\varphi(\mathbf{r}_2, t) \quad (12)$$

and the variable potential energy $\varphi(\mathbf{r}, t) = \varphi(\mathbf{r}) + \delta\varphi(\mathbf{r}, t)$, together with the Coulomb-matrix elements, gives a recipe

for the time evolution of the system (the dot denotes the time derivative):

$$\dot{d}_{ij}(t) = -\frac{i}{\hbar}\sum_{k<l} d_{kl}(t)\left\{V_{ijkl} - V_{ijlk} + \delta_{ijkl}(t)\right\} e^{\frac{i}{\hbar}(\mathcal{E}_{ij}-\mathcal{E}_{kl})t}, \tag{13}$$

with energy $\mathcal{E}_{ij} = \mathcal{E}_i + \mathcal{E}_j$ in the $|\tilde{ij}\rangle$ basis state. The matrix elements related to the potential energy are given by $\delta_{ijkl}(t) = \langle\tilde{ij}\,|\delta\varphi(\mathbf{r}_1,t) + \delta\varphi(\mathbf{r}_2,t)|\tilde{kl}\rangle = \delta\varphi_{ijkl}(t) - \delta\varphi_{ijlk}(t)$, where

$$\begin{aligned}\delta\varphi_{ijkl}(t) &= \langle ij\,|\delta\varphi(\mathbf{r}_1,t) + \delta\varphi(\mathbf{r}_2,t)|kl\rangle \\ &= \langle i|\delta\varphi(\mathbf{r},t)|k\rangle\delta_{jl} + \langle j\,|\delta\varphi(\mathbf{r},t)|l\rangle\delta_{ik}.\end{aligned} \tag{14}$$

The full time-dependent potential energy $\varphi(\mathbf{r},t) = \varphi(\mathbf{r}) + \delta\varphi(\mathbf{r},t)$ contains a variable component $\delta\varphi(\mathbf{r},t)$, generated by modulation of the gate voltages. The potential energy is calculated as $\varphi(\mathbf{r},t) = -|e|\phi(\mathbf{r},t)$, with the electrostatic potential $\phi(\mathbf{r},t)$ obtained by our solving the Poisson equation for the variable density $\rho(\mathbf{r},t)$ at every time step. The charge density originates from the actual wave function, and thus the Schrödinger and Poisson equations are solved in a self-consistent way.

G. Evaluation of valley indices

To follow the valley index corresponding to each dot, as well as the total valley index, we have to calculate the Fourier transform of the time-dependent two-electron wave function:

$$\begin{aligned}\tilde{\boldsymbol{\Psi}}(\mathbf{k}_1,\mathbf{k}_2,t) &= \int_F d^2r_1 d^2r_2\, \boldsymbol{\Psi}(\mathbf{r}_1,\mathbf{r}_2,t)e^{-i(\mathbf{k}_1\mathbf{r}_1+\mathbf{k}_2\mathbf{r}_2)} \\ &= \sum_{i<j} d_{ij}(t)\tilde{\boldsymbol{\Psi}}_{ij}(\mathbf{k}_1,\mathbf{k}_2)e^{-\frac{i}{\hbar}\mathcal{E}_{ij}t},\end{aligned} \tag{15}$$

with $\tilde{\boldsymbol{\Psi}}_{ij}(\mathbf{k}_1,\mathbf{k}_2) = [\tilde{\boldsymbol{\psi}}_i(\mathbf{k}_1)\tilde{\boldsymbol{\psi}}_j(\mathbf{k}_2) - \tilde{\boldsymbol{\psi}}_j(\mathbf{k}_1)\tilde{\boldsymbol{\psi}}_i(\mathbf{k}_2)]/\sqrt{2}$. For single-electron states $\boldsymbol{\psi}_i(\mathbf{r})$, the Fourier transform is defined as

$$\tilde{\boldsymbol{\psi}}_i(\mathbf{k}) = \int_F d^2r\, \boldsymbol{\psi}_i(\mathbf{r})e^{-i\mathbf{k}\mathbf{r}}, \tag{16}$$

integrated over the flake surface F, with the 2D wave vector $\mathbf{k} \equiv (k_x, k_y)$. The Fourier transform naturally exhibits periodicity in the reciprocal space, so we can restrict the k area to $\tilde{F}$: $k_{x,y} \in [-2\pi/a, 2\pi/a]$, which encompasses the first Brillouin zone.

Knowing $\tilde{\boldsymbol{\psi}}_i(\mathbf{k})$, we can calculate the probability density in the reciprocal space as

$$\begin{aligned}\tilde{\rho}(\mathbf{k},t) &= 2\int_{\tilde{F}} d^2k'\,|\tilde{\boldsymbol{\Psi}}(\mathbf{k},\mathbf{k}',t)|^2 \\ &= \sum_{i<j,k<l} d^*_{ij}(t)d_{kl}(t)\Big\{\tilde{\boldsymbol{\psi}}_i^{\dagger}(\mathbf{k})\tilde{\boldsymbol{\psi}}_k(\mathbf{k})\delta_{jl} - \tilde{\boldsymbol{\psi}}_i^{\dagger}(\mathbf{k})\tilde{\boldsymbol{\psi}}_l(\mathbf{k})\delta_{jk} \\ &\quad -\tilde{\boldsymbol{\psi}}_j^{\dagger}(\mathbf{k})\tilde{\boldsymbol{\psi}}_k(\mathbf{k})\delta_{il} + \tilde{\boldsymbol{\psi}}_j^{\dagger}(\mathbf{k})\tilde{\boldsymbol{\psi}}_l(\mathbf{k})\delta_{ik}\Big\} e^{\frac{i}{\hbar}(\mathcal{E}_{ij}-\mathcal{E}_{kl})t}.\end{aligned} \tag{17}$$

Finally, the total valley index of the two-electron system is calculated as

$$\mathcal{K}(t) = \frac{3a}{4\pi}\int_{\tilde{F}_{1/3}} d^2k\,\tilde{\rho}(\mathbf{k},t)k_x, \tag{18}$$

where the integration of the k_x component is performed over the reciprocal-space area $\tilde{F}_{1/3}$ defined as two opposite $\pi/3$ sectors within the $\tilde{F}$ area encompassing exactly one K point and one K' point (note that they have opposite k_x components). Point K (K') in $\tilde{F}_{1/3}$ has coordinates $1(-1)\times(4\pi/3a, 0)$, and thus the valley index for one electron would be in the interval $\mathcal{K}_{1e} \in [-1,1]$, with $\mathcal{K}_{1e} = 1$ representing the K valley, whereas $\mathcal{K}_{1e} = -1$ represents the K' valley. The total valley index spans the interval $\mathcal{K} \in [-2,2]$, with, for example, $\mathcal{K} = 2$ for the $|K_\downarrow K_\downarrow\rangle$ or $|K_\uparrow K_\uparrow\rangle$ state.

To get the expectation value of the valley isospin in each dot we have to collect the single-electron Fourier transforms (16), but now integrated over the left-dot area or the right-dot area; that is, we calculate $\tilde{\boldsymbol{\psi}}_i^{L}(\mathbf{k})$ $[\tilde{\boldsymbol{\psi}}_i^{R}(\mathbf{k})]$ by putting D_L (D_R) in the Fourier integral in Eq. (16). Then, by proceeding as before, we obtain the valley index in the left dot $\mathcal{K}_L(t)$ and the right dot $\mathcal{K}_R(t)$. Note that naturally $\mathcal{K}_L(R) \in [-1,1]$ becuase electrons are evenly distributed between both dots. To define two qubits, the electrons must occupy both dots simultaneously. In the other case, if both electrons occupied the same dot, the other, unoccupied one would have its qubit undefined.

IV. DOUBLE QUANTUM DOT

Knowing the double-dot confinement potential, we calculate a set of eigenstates of the Hamiltonian in Eq. (1) with the confinement potential energy $-|e|\phi$. These eigenstates are further used to build two-electron basis states [of the Slater determinant form given in Eq. (2)] for the two-qubit system considered. In Fig. 5, the subsequent single-electron eigenstates are presented for the double-dot potential from Fig. 4 albeit with a slightly higher barrier between the dots ($V_B = -1700$ mV), while the other voltages remain the same as in Fig. 4. We assign colors to the

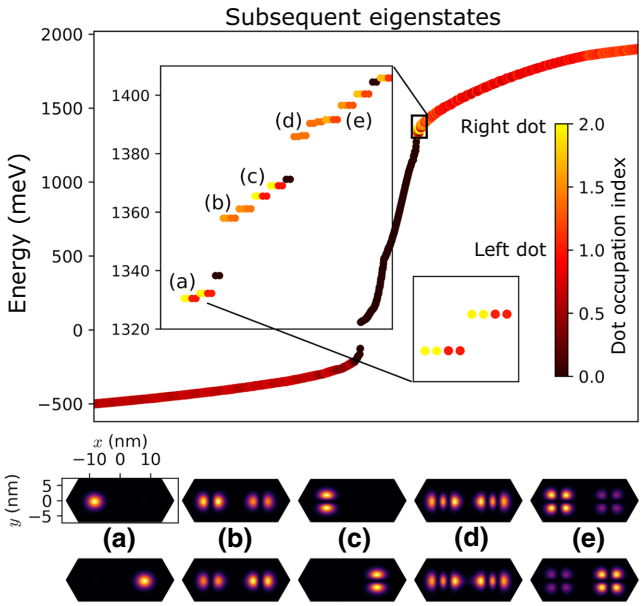

FIG. 5. (top) Single-electron states represented by markings on the energy scale with color that express electron localization: outside the dots, near the flake edges forming the "in-gap" states (black markings), and localized in the left dot (red) or the right dot (yellow). The insets show subsets of states located in the vicinity of the CB edge. Electron densities for states from groups (a)–(e) marked in the left inset are shown at the bottom.

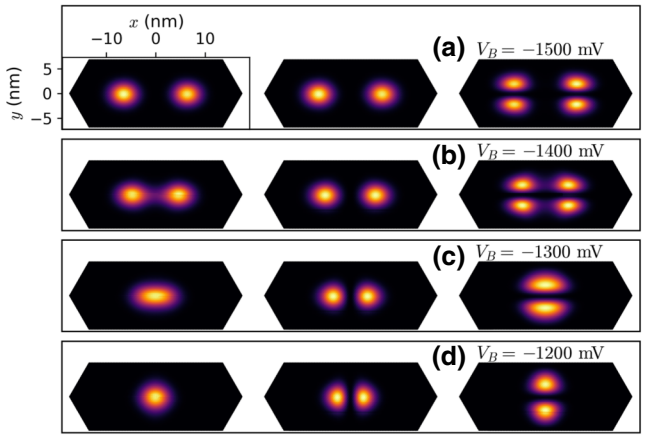

FIG. 6. Single-electron eigenstates for lower interdot barriers: (a) $V_B = -1500$ mV, (b) $V_B = -1400$, (c) $V_B = -1300$, and (d) $V_B = -1200$. Lowering the barrier between the dots makes the eigenstates spatially symmetric and antisymmetric.

dot occupancy parameter, defined as

$$\mathcal{N} = \int_{D_L} d^2r|\boldsymbol{\psi}_i(\mathbf{r})|^2 + 2\int_{D_R} d^2r|\boldsymbol{\psi}_i(\mathbf{r})|^2 \in [0,2], \quad (19)$$

with $\boldsymbol{\psi}_i$ being the ith eigenstate, D_L indicating the area over the left dot (but without including the edge), and D_R indicating the area over the right dot. Red markings mean that the electron is located in the left dot ($\mathcal{N} \simeq 1$), yellow markings mean that the electron is located in the right dot ($\mathcal{N} \simeq 2$), orange markings mean that the electron is evenly spread between both dots ($\mathcal{N} \simeq 1.5$), and black markings mean that the electron is outside the dots ($\mathcal{N} \simeq 0$). The latter means that the electron is in a state located at the edge of the flake, forming the so-called edge state. These edge states marked as black in Fig. 5 are forbidden for the electron confined within the dot, thus creating the band gap visible in Fig. 5 (left)—in the case of an infinite flake these states would disappear. It is also known that those states are not present in a torus geometry [72,73], equivalent to periodic boundary conditions, and their presence in open boundary conditions does not affect confined states in gate-defined regions in any way. We choose to keep open boundary conditions here due to our eight gate geometry, which ensures decoupling of qubits from the edge.

In the left inset in Fig. 5, we present several lowest states derived from the CB minimum at K, K' points. Some of them form characteristic yellow-red arrangements of four states [e.g., groups (a) and (c)], meaning that for the electron located in the left dot (red markings) we have two spin-orbit-split doublets (spin-valley subspace), and the same for the right dot (yellow markings). This gives eight states in total (see the right inset in Fig. 5).

On the other hand, some states are formed with symmetric densities and are marked in orange in Fig. 5 [e.g., groups (b) and (d)]. Electron densities of states from several groups, marked by (a)–(e) in the left inset, are presented on the right in Fig. 5. What is noteworthy is that bringing the dots closer to each other by modulating V_B, and thus lowering the interdot barrier, symmetrizes the eigenstates. They become spatially symmetric or antisymmetric, with the latter moving up on the energy scale. Electron densities for dots brought closer to each other are presented in Fig. 6. The left and center columns contain the lowest symmetric and antisymmetric states, respectively.

We now use the single-electron basis found for $V_B = -1300$ mV. The value of V_B is chosen so as to get spatially symmetric and antisymmetric states. This is motivated by the fact that we want to study and control interactions between two electrons in close proximity. To do so, we must set up a basis of antisymmetric Slater determinants given by Eq. (3). We take first 80 states from the CB minimum. In a basis so defined, we construct a matrix representing the two-electron Hamiltonian from Eq. (5) with the Coulomb interaction via the configuration-interaction method, filled by single-electron eigenenergies $\mathcal{E}_i + \mathcal{E}_j = \mathcal{E}_{ij}$ and Coulomb two-electron matrix elements V_{ijkl} as in Eq. (8). We solve the eigenproblem by the exact diagonalization of the constructed H_{2e} matrix. The key parameter that controls coupling between electrons is the barrier height controlled by the voltage V_B.

In Fig. 7 we present the first 16 two-electron eigenstates spanning a spin- and valley-degenerate subspace [18], with

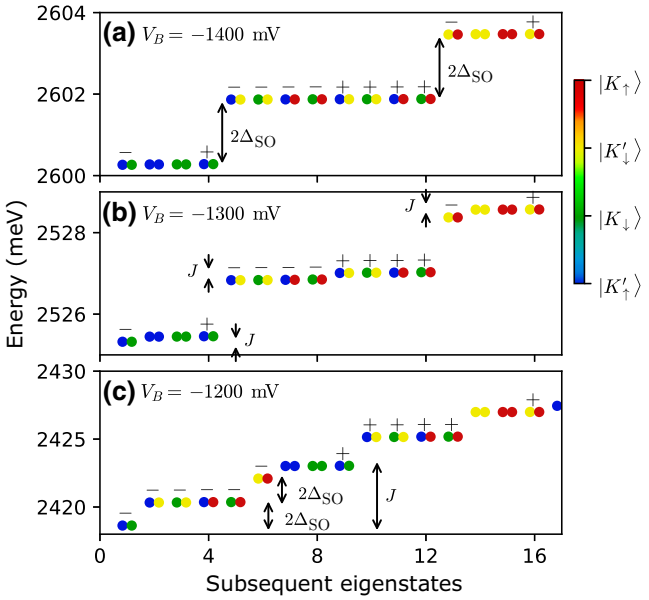

FIG. 7. Two-electron states for different coupling between the dots, controlled via voltages $V_B = V_3 = V_7$, giving three regimes of the interplay between the exchange energy and spin-orbit splitting: (a) $J \ll 2\Delta_{SO}$, (b) $J < 2\Delta_{SO}$, and (c) $J > 2\Delta_{SO}$. These 16 lowest states span the ground two-electron spin-valley-degeneracy subspace. We identify them as built up mainly from the first four single-electron CB states: $|K'_\uparrow\rangle$, $|K_\downarrow\rangle$, $|K'_\downarrow\rangle$, $|K_\uparrow\rangle$, colored in blue, green, yellow, and red, respectively. The minus or plus signs above pairs of dots, which represents an eigenstate, denote the singlet or the T_0-triplet combinations.

the same (in the limit of decoupled dots) spatial state, being the ground state (with closer dots this state becomes a spatial symmetric-antisymmetric pair). They are built up mainly (but not exactly, because in our exact calculations we use the full Coulomb interaction) from the first four single-electron states from the CB edge (spin-valley degeneracy): $\{|K'_\uparrow\rangle, |K_\downarrow\rangle, |K'_\downarrow\rangle, |K_\uparrow\rangle\}$, split by the spin-orbit-coupling energy Δ_{SO}. We identify them by calculating the total spin (see Appendix D) and the total valley index $\mathcal{K}$, defined in Eq. (18).

The first four states form the singlet-triplet base $\{|K'_\uparrow K_\downarrow\rangle - |K_\downarrow K'_\uparrow\rangle, |K'_\uparrow K'_\uparrow\rangle, |K'_\uparrow K_\downarrow\rangle + |K_\downarrow K'_\uparrow\rangle, |K_\downarrow K_\downarrow\rangle\}$ split by the spin-valley exchange energy J. Singlets are denoted in Fig. 7 by a minus sign above a pair of dots representing the given state, while T_0 triplets are denoted by plus signs. The next eight states, four singlets and four T_0 triplets, are separated by the doubled single-electron spin-orbit-splitting value ($2\Delta_{SO}$). The next four states also form a singlet-triplet set, but are made of the two upper states: $\{|K'_\downarrow\rangle, |K_\uparrow\rangle\}$. By lowering $|V_B|$ from $V_B = -1400$ mV in Fig. 7(a) to $V_B = -1200$ in Fig. 7(c), we observe that states are gradually reorganized on the energy scale. It is clear that V_B controls the interdot exchange: for $V_B = -1400$ mV, $J \ll 2\Delta_{SO}$, while for $V_B = -1200$, the exchange dominates: $J > 2\Delta_{SO}$.

When one is analyzing two-electron states, it is also sensible to examine the dependence of eigenenergies on the applied external magnetic field [88]. To calculate the energy spectrum in such a case, we add to the Hamiltonian in Eq. (1) the standard Zeeman term:

$$H_Z = \sum_{i\sigma\sigma'\alpha\beta} \gamma_Z \mathbf{B} \cdot \mathbf{s}_{\sigma\sigma'} \delta_{\alpha\beta} \hat{c}^\dagger_{i\alpha\sigma} \hat{c}_{i\alpha\sigma'}, \tag{20}$$

with the magnetic field $\mathbf{B}$. For $\gamma_Z = g_e \mu_B/2$, we arrive at the Zeeman energy $g\mu_B \mathbf{s} \cdot \mathbf{B}/2$. To also address the spatial effects related to the magnetic field, we apply the so-called Peierls substitution [101]. We multiply the hopping matrix by the additional factor $t_{ij} \to \tilde{t}_{ij} = t_{ij} \exp i\theta_B$ in the Hamiltonian in Eq. (1). Now the vector potential $\mathbf{A}$ (we use the Landau gauge, $\mathbf{A} = [0, B_z x, 0]^T$, for the perpendicular magnetic field $\mathbf{B} = [0, 0, B_z]^T$) enters Eq. (1) via the Peierls phase θ_B, calculated as the path integral between neighboring nodes: $\theta_B = e/\hbar \int \mathbf{A} \cdot d\mathbf{r}$.

The most-noticeable result of applying a magnetic field is the splitting, introduced between levels with opposite total spin and/or valley index. In the first four states (1–4) and the last four states (13–16) [numbering as in Fig. 7(a)], the singlet S and triplet T_0 have opposite spins and valley indices, meaning that their energy is almost constant in the magnetic field. Two T_+ and T_- triplet states are split in the magnetic field, the upper pair (14, 15) more strongly than the lower pair (2, 3). In the eight states in the middle we have S and T_0 composed of pairs with opposite spins or opposite valleys, which manifests itself in a different magnetic field dependence, with g factors that are different for spin and valley indices; that is, in MoS_2, $g_v > g_s$ [19].

V. VALLEY MANIPULATION AND EXCHANGE

A. Single-qubit operations

So far we have described the calculation method to determine the evolution of the system wave function under an applied external electrostatic potential via local gating, as well as to determine the dressed eigenspectrum of the two-electron system. Moreover, we have described a method for calculating valley isospin in each dot separately (left or right). Now we are ready to define a two-qubit system based on the valley degree of freedom in each dot: left and right. To disentangle the valley degree of both electrons from their spins, we apply an external magnetic field, arriving at a work subspace of, let us say, spin-up states, $\{|K'_\uparrow\rangle, |K_\uparrow\rangle\}$, for each electron. This magnetic field also enables us to set the specific frequency of valley transitions within the given spin subspace [19]. This way, the lowest (red dot) state in Fig. 8, $|K'_\uparrow K'_\uparrow\rangle$, represents the $|00\rangle$ two-qubit state, with $\mathcal{K}_L = \mathcal{K}_R = -1$, while the linear combination of the singlet and triplet (orange

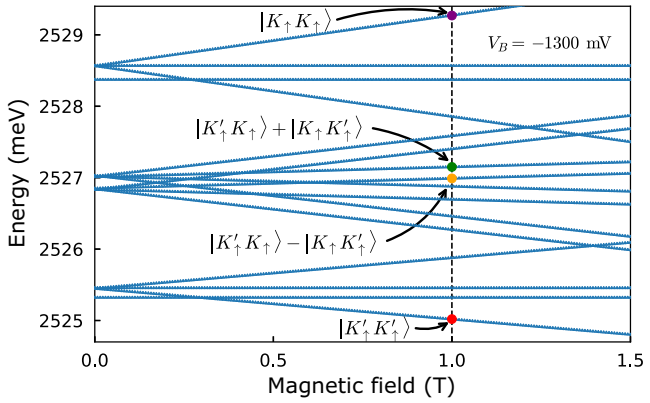

FIG. 8. Evolution of the two-electron states from Fig. 7(b) (i.e., for $V_B = -1300$) in an external magnetic field. Red, orange, green, and violet dots represent states that span the two valley-qubit subspace (with the spin up) for the applied perpendicular magnetic field $B_z = 1$ T.

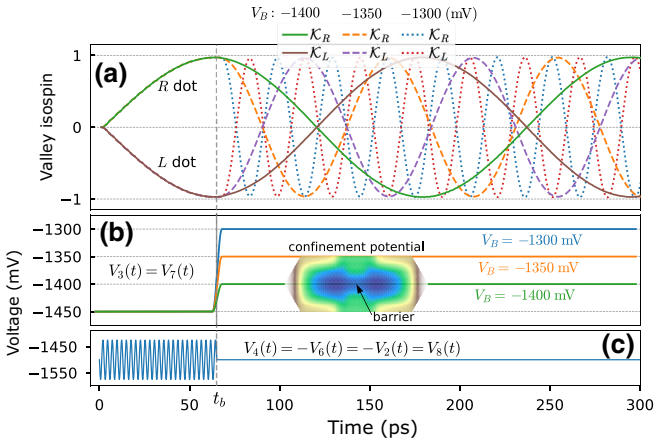

FIG. 9. (a) Evolution of the two-qubit system. In the first step, at $0 < t < t_b = 64$ ps, modulated voltages at nearby gates (c) induce the left (right) valley-qubit rotations, depicted by the brown (green) curve, after which we arrive at opposite valley states: $\mathcal{K}_L = -1$ and $\mathcal{K}_R = 1$. In the second step, for $t > t_b$, we reduce the interdot barrier by raising the voltage V_B, and observe the valley exchange between the dots, which can be seen as the (two-qubit) valley-swap operation. (b) Raising V_B up to three different levels at $t_b = 64$ ps reduces the interdot barrier, couples the dots, and induces the valley exchange with three different exchange periods, as in (a).

and green dots in Fig. 8), with a plus sign or a minus sign, gives a $|01\rangle$ state ($\mathcal{K}_L = -1$, $\mathcal{K}_R = 1$) or a $|10\rangle$ state ($\mathcal{K}_L = 1$, $\mathcal{K}_R = -1$). The violet dot represents the $|11\rangle$ state, with $\mathcal{K}_L = \mathcal{K}_R = 1$. Remember that we define qubits not on indistinguishable electrons, which are described by an antisymmetric wave function, but on the valley index of localized, spatially separated dots.

Because qubits are localized in different dots, we can easily manipulate them electrically, addressing their valley indices separately, by applying an oscillating voltage to the local gates in each dot separately [17]. Now we show how this is done in our two-qubit device. We assume that initially the system is in the singlet state within the spin-up subspace, meaning that the valley index in each dot is zero and each qubit is in the equally weighted superposition of K and K' states (orange or green dots in Fig. 8).

We start the time evolution governed by Eq. (13) and turn on oscillating voltages on gates G_4 and G_6 next to the left dot: $V_4(t) = -V_6(t) = V_{\rm ac} \sin \omega t$, $V_{\rm ac} = 75$ mV. The pumping frequency $\omega = 1/T$, where $T = 2.37$ ps [see Fig. 9(c)], is tuned to the energy splitting, which equals the spin-orbit splitting $2\Delta_{\rm SO} = 1.75$ meV for $B_z = 0$. However, for $B_z = 1$ T, the energy splitting (energy difference between the red and green dots in Fig. 8) is a bit larger, and is about 1.95 meV, due to additional valley-Zeeman splitting [19] between these two valley states, which at the same time are the qubit basis states. This way, by modulating the confinement potential in the left-dot area, we induce a transition between the valley states of the left qubit, and thus rotate the $|\mathcal{K}_L\rangle$ qubit [17]. The valley index calculated for the left dot $\mathcal{K}_L$ (i.e., defined in the same way as the total valley index in Eq. (18), but calculated for the Fourier transforms integrated over the left dot) is depicted in Fig. 9(a) by a brown curve. One can observe a gradual decrease from 0 to -1, meaning that after time $t_b = 64$ ps the left qubit is in the K' state. A similar situation happens in the right dot, where the potential is also modulated by an additional oscillating voltage applied to gates G_2 and G_8 (forming the potential of the right dot) albeit in antiphase: $V_2(t) = -V_8(t) = -V_{\rm ac} \sin \omega t$ [see Fig. 9(c)]. The aforementioned modulation also results in an intervalley transition in the right dot (green curve), and finally at t_b the right qubit is in the K state with a valley index of 1: $|\mathcal{K}_R = 1\rangle$. The voltages in the dots oscillate in antiphase with the purpose to obtain antiparallel qubits at the end of this evolution step.

B. Two-qubit operation

During the previous step (for $0 < t < t_b$), the barrier between the dots was set to be high [$V_3(t) = V_7(t) = -1450$ mV], ensuring that no valley isospin exchange between left and right dots occurs. We have shown how to perform single-qubit operations on individual qubits by manipulating voltages applied to nearby gates. To fulfill the universality criterion [102] we also need to implement a two-qubit operation. The simplest one, which naturally emerges in a system of two isospins, is their exchange, or SWAP using quantum-information language. It is known that the $\sqrt{\rm SWAP}$ gate, which performs half of a two-qubit swap, is universal in a sense that any multiqubit gate can be constructed from only $\sqrt{\rm SWAP}$ and single-qubit gates [103].

Now at time $t_b = 64$ ps we lower the interdot barrier by raising the (negative) voltage V_B, as shown in Fig. 9(b), and thus begin swapping the valley isospins between the dots. The modulation of voltages on gates G_2 and G_8 and on gates G_4 and G_6 is now turned off. In Fig. 9(a) we observe that valley indices between dots $\mathcal{K}_L$ and $\mathcal{K}_R$ exchange their values. What is characteristic is that this process is faster when the barrier, controlled by V_B, is lower. In other words, the barrier height controls the coupling between the dots. We perform simulations for three different barrier heights. For $V_B = -1400$ mV (brown and green curves) the swap is completed in $T_{\mathrm{SWAP}} = 230$ ps, for -1350 mV (violet and orange curves) in 94 ps, while for -1300 mV (red and blue curves) it takes 30 ps. The exchange time translates to singlet-triplet energy difference $J = h/T_{\mathrm{SWAP}}$, which agrees with the exchange energies 20, 45, and 125 μeV, respectively, obtained from the two-electron eigenspectrum presented in Fig. 7. Thus, the $\sqrt{\mathrm{SWAP}}$-gate timings, which last half of T_{SWAP}, are relatively short—we can perform a full operation cycle within less than 100 ps. This time can be tuned precisely by adjustment of the interdot barrier height via the voltages $V_B = V_3 = V_7$.

We assume the singlet state is the starting state of our simulation, but this is not the only option. With magnetic field $B_z = 1$ T, the lowest state is the polarized triplet $|K'_\uparrow K'_\uparrow\rangle$ (see Fig. 8). We could also assume this state is the starting state. Then, to observe the exchange, in the first stage of the operation we have to rotate the valley in only one dot. As a result, we would also get two opposite valleys, and would then be able to observe their exchange.

VI. SINGLE-SHOT READOUT VIA PAULI BLOCKADE

To get a complete physical implementation of the quantum computer, apart from single-qubit operations and swapping, we need the ability to initialize the state of the qubits as well as a qubit-specific measurement capability. Among numerous spin initialization and readout methods in gated QDs, the most-common approach is to use the Pauli-spin-blockade mechanism [104,105].

In the following paragraphs, we show that the Pauli-blockade effect can be extended in our setting to the valley degree of freedom, similarly as was done for carbon nanotubes [22,106]. In Pauli blockade, a double quantum dot containing two electrons in total is tuned to the transition between two charge states: (1,1) with one electron in each dot and (0,2) with both electrons in the right dot. This transition involves the electron tunneling from the left dot to the right dot. If we properly tune the voltage bias between the dots, we set a blockade for the (1,1)-valley-triplet state, for which transition to an energetically accessible (0,2)-valley-singlet state is forbidden. It is crucial that the (0,2)-valley-triplet state, which would not block, is sufficiently separated in energy by the (0,2)-singlet-triplet energy difference, which in our case is about 5 meV. On the other hand, the (1,1)-valley-singlet state in this regime is not blocked. The cases discussed above are presented in Fig. 10. To observe the blockade we add a positive offset voltage $V_{\mathrm{bias}} > 0$ between the dots by raising the voltage V_1: $\tilde{V}_1(t) = V_1 + V_{\mathrm{bias}}$. Then we stimulate an electron transition from the left dot to the right dot, the lower one (see the blue potential profile in Fig. 10), by applying an additional oscillating voltage to gate G_5: $\tilde{V}_5(t) = V_5 + V_{\mathrm{stim}} \sin \omega_{\mathrm{stim}} t$, where $V_{\mathrm{stim}} = 5$ mV and $2\pi/\omega_{\mathrm{stim}} = 5$ ps. When simulating the blockade, we take slightly different single-electron eigenstates, obtained for $V_1 = -1550$ mV and $V_B = -1300$ mV, while the other voltages remain the same as in Fig. 4. This step aims to add states with asymmetric densities (located majorly in the right dot) to the basis.

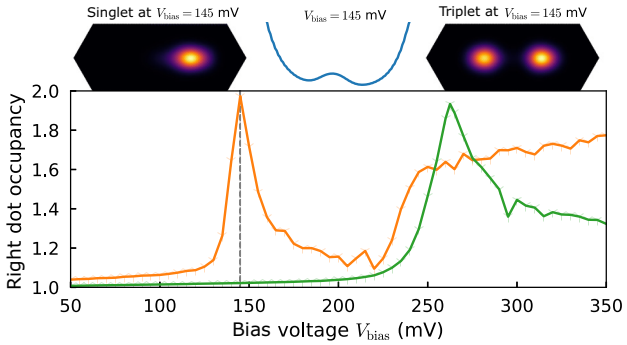

FIG. 10. Valley Pauli blockade. The right-dot occupancy at various biasing voltages, calculated for the singlet initial state (orange) and the triplet initial state (green), shows resonance (which means increased transition between the dots) at different biases. This way, proper biasing (i.e., $V_{\mathrm{bias}} = 145$ mV) enables electron transfer in the singlet state but blocking in the triplet state.

After turning on $V_{\mathrm{stim}} \sin \omega_{\mathrm{stim}} t$, we gradually increase V_{bias} and calculate time evolutions for each of the V_{bias} values considered and for two different initial two-electron states: singlet $|K'_\uparrow K_\downarrow\rangle - |K_\downarrow K'_\uparrow\rangle$ and triplet $|K'_\uparrow K'_\uparrow\rangle$. After a few dozen picoseconds, we observe that for the singlet initial state and $V_{\mathrm{bias}} = 145$ mV the "left electron" transfers completely to the right dot (nonblocked state), while for the triplet state the occupancy of both dots is almost unchanged (blocked state). The resulting electron densities for the singlet (triplet) state are presented at the top left (top right) in Fig. 10. The occupancy of the right dot, calculated as the total electron density $\rho(\mathbf{r})$ (defined in Appendix D) integrated over the right dot, does not remain constant after the transfer. The density oscillates over time as the electron goes back and forth between the dots, and the occupancy plot, presented in Fig. 10, shows their maximum values over time. It is now clear that for the singlet state (orange curve) and for the triplet state (green curve) the resonant

transitions occur at different biasing: $V^S_{\rm bias} = 145$ mV and $V^T_{\rm bias} = 265$ mV, respectively. Thus, at $V_{\rm bias} = V^S_{\rm bias}$, we observe the valley Pauli blockade for the electron density defining the left valley qubit. The estimated blockade fidelity is about 97.5%.

Therefore, using the valley blockade, one can set up or read out the left valley-qubit state. However, we should keep in mind that the spin degree of freedom makes the (spin-valley) singlet-triplet subspace extend to 16 states (not just $1+3$). This complicates proper setting up of the Pauli blockade. To resolve valley from spin, we have to apply a magnetic field, and then use of proper transition frequencies, as in Fig. 8, of the valley single-qubit operations ensures that we stay within the given spin (let us say, up) subspace. But how can we initialize or check that two qubits are in the desired valley state *together* with the given spin? A magnetic field enriches the blockade operation [107]. If we look at Fig. 8, we see that for $B_z = 1$ T the analyzed triplet $|K'_\uparrow K'_\uparrow\rangle$ and singlet $|K'_\uparrow K_\downarrow\rangle - |K_\downarrow K'_\uparrow\rangle$ are the two lowest states. By proper adjustment the left lead potential [i.e., to energy lower than the third state $|K'_\uparrow K_\downarrow\rangle + |K_\downarrow K'_\uparrow\rangle$ (unwanted triplet)], we allow only these two (1,1) states to populate the double dot. This way we ensure that only $|K_\uparrow K_\uparrow\rangle$ is blocked, thus implementing the valley-qubit initialization.

VII. SUMMARY

We study a two-electron system in a gate-defined TMDC double quantum dots from the point of view of valley-qubit implementation. Using the configuration-interaction method, the realistic theory of Coulomb interaction, and the time-dependent Schrödinger equation coupled with the Poisson equation, which models a realistic dielectric environment, we describe a proposed nanodevice with an eight-gate geometry and time-modulated electric potentials.

By performing numerical simulations, we show how one can obtain single-qubit and two-qubit gates in the valley two-qubit system by electrically controlling the state of the electrons and the interdot coupling in a static magnetic field. First, we explain each qubit rotation (single-qubit operations) in the left dot or the right dot, controlled separately by the local gates. Then, we couple both qubits, getting the valley swap (two-qubit operation). Finally, we discuss how to setup the valley Pauli blockade to implement the valley-qubit initialization and readout. In this way, we obtain a physical scheme to realize universal quantum computation based on valley isospin in the gate-defined TMDC double quantum dots.

In our theoretical description of the two-electron system, we use the exact configuration-interaction method, which gives a basis of dressed states in an interaction between the electrons. The Coulomb interaction and the confinement potential are modeled realistically, including atomic matrix elements, the screening by nearby dielectric layers, and voltages applied to the layout of control gates with geometry inspired by experiments. Variable control voltages modulate the confinement potential, leading to nontrivial device operation calculated with the time-dependent Schrödinger equation and solved in the configuration-interaction basis self-consistently with the Poisson equation.

ACKNOWLEDGMENTS

The authors thank Dariusz Żebrowski and Paweł Potasz for invaluable discussions. This work was supported by the polish National Science Centre under Grant No. 2016/20/S/ST3/00141. T.W. acknowledges financial support from the Polish Ministry of Science and Higher Education via Grant No. D/2015/002645. M.B. acknowledges financial support from the Polish National Science Centre under Maestro Grant No. 2014/14/A/ST3/00654. This research was supported in part by PL-Grid Infrastructure, Wrocław Center for Networking and Supercomputing and Compute Canada.

APPENDIX A: TWO-ELECTRON HAMILTONIAN

Here we present an explicit derivation of the formula for the Hamiltonian in Eq. (5):

$$
\begin{aligned}
&\sum_{i<j,k<l} |\tilde{ij}\rangle\langle\tilde{ij}|H_{2e}|\tilde{kl}\rangle\langle\tilde{kl}| \\
&= \sum_{i<j,k<l} |\tilde{ij}\rangle\langle\tilde{kl}| \left[\mathcal{E}_{ij}\left(\delta_{ik}\delta_{jl} - \delta_{il}\delta_{jk}\right) + \langle\tilde{ij}|\bar{V}_C|\tilde{kl}\rangle\right] \\
&= \sum_{i<j,k<l} d_i^\dagger d_j^\dagger |\tilde{0}\rangle\langle\tilde{0}| d_k d_l \Big[\mathcal{E}_{ij}\,\delta_{ik}\delta_{jl} \\
&\quad + \langle ij|\bar{V}_C|kl\rangle - \langle ij|\bar{V}_C|lk\rangle\Big] \\
&= \sum_{i<j} d_i^\dagger d_j^\dagger |\tilde{0}\rangle\langle\tilde{0}| d_i d_j\, \mathcal{E}_{ij} \\
&\quad + \sum_{i<j,k<l} d_i^\dagger d_j^\dagger |\tilde{0}\rangle\langle\tilde{0}| d_k d_l \left(V_{ijkl} - V_{ijlk}\right).
\end{aligned}
$$

The two-electron energy is simply the sum of the single-electron-state energies: $\mathcal{E}_{ij} = \mathcal{E}_i + \mathcal{E}_j$. Note that, firstly, $\delta_{il}\delta_{jk}$ vanishes since $i<j$, $k<l$. Secondly, we have $\langle\tilde{ij}|\bar{V}_C|\tilde{kl}\rangle = \langle ij|\bar{V}_C|kl\rangle - \langle ij|\bar{V}_C|lk\rangle$, so we introduce the abbreviation $\langle ij|\bar{V}_C|kl\rangle \equiv V_{ijkl}$.

APPENDIX B: ATOMIC COULOMB ELEMENTS

In this section we present numerical values for the atomic Coulomb-matrix elements. We use the following numbering of orbitals: $\alpha = 1,2,3$ for the Mo d_{z^2}, d_{xy}, and $d_{x^2-y^2}$ orbitals, respectively.

TABLE I. The largest Coulomb atomic integrals with the listed largest energies from each group (eV). We include only elements with energies larger than 0.3 eV, while the others are taken classically, as interaction between two point charges. Each two-center integral occurs six times, one for each R_1–R_6 direction.

Group	One-center integrals $\langle ss\|V_C^0\|ss\rangle$	
1	14.43	$\langle s^\alpha s^\alpha\|V_C^0\|s^\alpha s^\alpha\rangle$, $\alpha = 1,2,3$
2	13.63	$\langle s^2s^3\|V_C^0\|s^2s^3\rangle$, $\langle s^3s^2\|V_C^0\|s^3s^2\rangle$
3	12.86	$\langle s^1s^2\|V_C^0\|s^1s^2\rangle$, $\langle s^2s^1\|V_C^0\|s^2s^1\rangle$, $\langle s^1s^3\|V_C^0\|s^1s^3\rangle$, $\langle s^3s^1\|V_C^0\|s^3s^1\rangle$
7	0.79	$\langle s^1s^2\|V_C^0\|s^2s^1\rangle$, $\langle s^2s^1\|V_C^0\|s^1s^2\rangle$, $\langle s^1s^3\|V_C^0\|s^3s^1\rangle$, $\langle s^3s^1\|V_C^0\|s^1s^3\rangle$, $\langle s^1s^1\|V_C^0\|s^2s^2\rangle$, $\langle s^2s^2\|V_C^0\|s^1s^1\rangle$, $\langle s^1s^1\|V_C^0\|s^3s^3\rangle$, $\langle s^3s^3\|V_C^0\|s^1s^1\rangle$
8	0.41	$\langle s^2s^3\|V_C^0\|s^3s^2\rangle$, $\langle s^3s^2\|V_C^0\|s^2s^3\rangle$, $\langle s^2s^2\|V_C^0\|s^3s^3\rangle$, $\langle s^3s^3\|V_C^0\|s^2s^2\rangle$
	Two-center integrals $\langle sp\|V_C^0\|sp\rangle$	
4	4.71	$\langle s^2p^2\|V_C^0\|s^2p^2\rangle$, $\langle s^3p^3\|V_C^0\|s^3p^3\rangle$, $\langle s^2p^3\|V_C^0\|s^2p^3\rangle$, $\langle s^3p^2\|V_C^0\|s^3p^2\rangle$
5	4.55	$\langle s^1p^2\|V_C^0\|s^1p^2\rangle$, $\langle s^2p^1\|V_C^0\|s^2p^1\rangle$, $\langle s^1p^3\|V_C^0\|s^1p^3\rangle$, $\langle s^3p^1\|V_C^0\|s^3p^1\rangle$
6	4.42	$\langle s^1p^1\|V_C^0\|s^1p^1\rangle$

When calculating the one-center ($\mathbf{r}_s = \mathbf{r}_p$) and two-center ($\mathbf{r}_s \neq \mathbf{r}_p$) integrals listed in Table I, we take the three-dimensional Coulomb interaction in a vacuum, $V_C^0(r) = (|e|^2/4\pi\varepsilon_0 r)$. The values obtained are then renormalized by the $\mathrm{rn}(|\mathbf{r}_s - \mathbf{r}_p|)$ function defined in Appendix C, and this way we estimate $\mathcal{V}_{spdf}$ values, defined in Eq. (10), for the *screened* Coulomb interaction:

$$\langle s^{\alpha_s}p^{\alpha_p}|\bar{V}_C|s^{\alpha_d}p^{\alpha_f}\rangle \simeq \frac{\langle s^{\alpha_s}p^{\alpha_p}|V_C^0|s^{\alpha_d}p^{\alpha_f}\rangle}{\kappa\ \mathrm{rn}(|\mathbf{r}_s - \mathbf{r}_p|)}. \tag{B1}$$

This way we include the screening effects of the dielectric environment (nearby insulators) and the monolayer flake. The calculated integrals, shown in Fig. 11 and listed in Table I, do not take into account screening, and can be applied to other structures with, for example, different insulating layers.

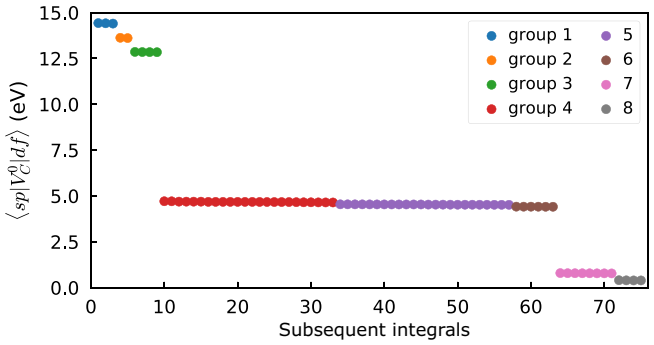

FIG. 11. Interaction energies for subsequent groups of integrals as listed in Table I.

APPENDIX C: COULOMB EFFECTIVE INTERACTION

We now introduce the screened Coulomb potential used in our model. We check three different approaches to describe the screened Coulomb interaction in 2D structures, and verify them with an exact numerical potential calculated for our structure.

In the simplest, naive, approach at the flake level, we take ε as the average from two neighboring materials: $\kappa = (\varepsilon_{h\text{-BN}} + \varepsilon_{\mathrm{SiO_2}})/2 = 4.5$ (in ε_0 units) [108]. We assume the following dielectric constants: $\varepsilon_{h\text{-BN}} = 5.1$ (for the top layer of hexagonal boron nitride) [109] and $\varepsilon_{\mathrm{SiO_2}} = 3.9$ (for the bottom layer of quartz). However, the following potential derived by Keldysh [110,111] to model the Coulomb interaction in a thin semiconductor layer embedded between top and bottom layers with given permittivity is much-more accurate:

$$V_K(r) = \frac{|e|^2}{4\pi\varepsilon_0}\frac{\pi}{2r_0}\left[H_0\left(\frac{\kappa r}{r_0}\right) - Y_0\left(\frac{\kappa r}{r_0}\right)\right], \tag{C1}$$

with the zero-order Struve function and the Bessel function of the second kind. Another potential, V_{TYD}, was introduced by Tuan, Yang, and Dery (TYD) [112] to better model the Coulomb interaction in TMDC monolayers. In addition to information about the permeability of adjacent dielectric layers, it takes into account the values of the polarizabilities χ_+ of the central Mo atomic sheet and χ_- for the top and bottom S (chalcogen) sheets. We take the following parameters for the Keldysh and TYD potentials: $\kappa = (\varepsilon_t + \varepsilon_b)/2 = (\varepsilon_{h\text{-BN}} + \varepsilon_{\mathrm{SiO_2}})/2 = 4.5$ (ε_0), $r_0 = 7.5d = 4.875$ nm, $l_+ = 2\pi\chi_+ = 5.6d = 3.64$ nm, and $l_- = 2\pi\chi_- = 5d = 3.25$ nm ($d = 0.65$ nm for MoS_2). See Ref. [112] for a detailed analysis of the fitting parameters for these models.

We compare all of these model potentials with the standard three-dimensional Coulomb potential $V_C(r) = V_C^0(r)/\kappa = (|e|^2/4\pi\varepsilon_0)(1/\kappa r)$ and the potential $V_N(r)$ calculated numerically via the Poisson equation for the space-dependent permittivity,

$$\kappa(z) = \begin{cases} \varepsilon_{h\text{-BN}} & \text{for} \quad z > d/2, \\ 1 & \text{for} \quad -d/2 < z < d/2, \\ \varepsilon_{\mathrm{SiO_2}} & \text{for} \quad z < -d/2, \end{cases} \tag{C2}$$

and the average 2D polarizability for the MoS_2 monolayer taken as $\chi = 0.55$ nm, which screens the electron charge in the monolayer itself, weakening it by the factor $\varepsilon = 1 + (4\pi\chi/d) \simeq 12$ [113,114].

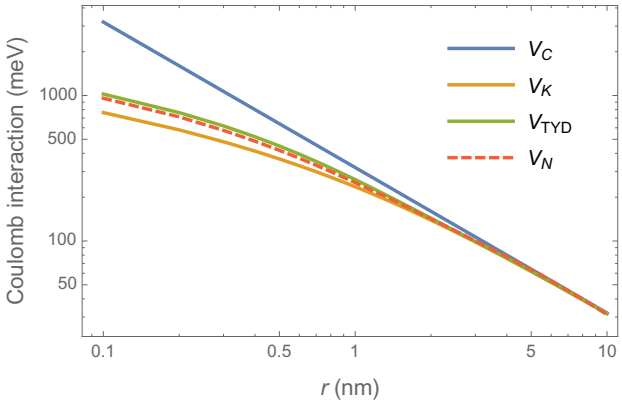

FIG. 12. The screened Coulomb interaction captured by several model potentials, and compared with the exact numerical result $V_N(r)$. Comparison between the Coulomb potential $V_C(r)$ and best potential $V_{\mathrm{TYD}}(r)$ gives a correction for screening, described by the $\mathrm{rn}(r)$ function.

A comparison of all the potentials is presented in Fig. 12. We can see that the Keldysh, TYD, and numerical potentials give qualitatively comparable results, while the bare Coulomb potential overestimates the interaction, especially at small distances ($r < 1$ nm). The closest results to the numerical results are obtained with the TYD potential, and we take that potential to describe the electron-electron interaction in our model:

$$\bar{V}_C(r) = V_{\mathrm{TYD}}(r) \simeq \frac{V_C^0(r)}{\kappa\ \mathrm{rn}(r)}. \tag{C3}$$

We are now able to define the function that renormalizes the bare Coulomb potential to describe realistic screening: $\mathrm{rn}(r) = V_C(r)/V_{\mathrm{TYD}}(r)$. The exact analytical formula for the TYD potential is rather complicated; thus, for convenience, we approximate $\mathrm{rn}(r)$ using the following formula: $\mathrm{rn}(r) \simeq (r + 0.2/r - 0.01)$, $r > 0.01$ (r is in nanometers). This means that, for example, for $r = 0.319$ nm we have to divide the energies obtained from the Monte Carlo approach (listed in Table I) by 1.68 (times κ). On the other hand, for interaction at the same node, for one-center integrals, we need to divide the energies by about 3 (assuming the average radius of the Mo atom). However, if we take into account the fact that for atomic length scales the screening naturally decreases (in contrast to a simple model of dielectric slabs), then for $r \sim d$ the real ϵ is (roughly speaking) about twice as small [113]. Hence, for interaction on the node itself, we assume 1.5 instead of 3: $\mathrm{rn}(r \simeq 0) = 1.5$.

APPENDIX D: TWO-ELECTRON DENSITY AND TOTAL SPIN

The full two-electron wave function is expanded in the configuration-interaction basis as

$$\boldsymbol{\Psi}(\mathbf{r}_1, \mathbf{r}_2) = \sum_{i<j} d_{ij}\ \boldsymbol{\Psi}_{ij}(\mathbf{r}_1, \mathbf{r}_2). \tag{D1}$$

Thus, expansion for the total electron density reads

$$\begin{aligned}\rho(\mathbf{r}) &= \int d\mathbf{r}' |\boldsymbol{\Psi}(\mathbf{r}, \mathbf{r}')|^2 + |\boldsymbol{\Psi}(\mathbf{r}', \mathbf{r})|^2 = 2\int d\mathbf{r}' |\boldsymbol{\Psi}(\mathbf{r}, \mathbf{r}')|^2 \\ &= 2\sum_{i<j,k<l} d_{ij}^* d_{kl} \int d\mathbf{r}' \boldsymbol{\Psi}_{ij}^\dagger(\mathbf{r}, \mathbf{r}') \boldsymbol{\Psi}_{kl}(\mathbf{r}, \mathbf{r}') \\ &= \sum_{i<j,k<l} d_{ij}^* d_{kl} \Big\{ \boldsymbol{\psi}_i^\dagger(\mathbf{r}) \boldsymbol{\psi}_k(\mathbf{r}) \delta_{jl} - \boldsymbol{\psi}_i^\dagger(\mathbf{r}) \boldsymbol{\psi}_l(\mathbf{r}) \delta_{jk} \\ &\quad - \boldsymbol{\psi}_j^\dagger(\mathbf{r}) \boldsymbol{\psi}_k(\mathbf{r}) \delta_{il} + \boldsymbol{\psi}_j^\dagger(\mathbf{r}) \boldsymbol{\psi}_l(\mathbf{r}) \delta_{ik} \Big\},\end{aligned}$$

where for clarity we omit the $\otimes$ symbol. Because of the antisymmetry constraint $\Psi_{ij}^{\sigma_i\alpha_i\sigma_j\alpha_j}(\mathbf{r}', \mathbf{r}) = -\Psi_{ij}^{\sigma_j\alpha_j\sigma_i\alpha_i}(\mathbf{r}, \mathbf{r}')$, we get $|\boldsymbol{\Psi}(\mathbf{r}', \mathbf{r})|^2 = |\boldsymbol{\Psi}(\mathbf{r}, \mathbf{r}')|^2$. Obviously one has $\int d\mathbf{r}\, \rho(\mathbf{r}) = 2$. The total spin is calculated in the same way:

$$\begin{aligned}\langle \sigma_z \rangle &= \langle \boldsymbol{\Psi} | \boldsymbol{\sigma}_z \otimes \mathbf{1} + \mathbf{1} \otimes \boldsymbol{\sigma}_z | \boldsymbol{\Psi} \rangle = 2 \langle \boldsymbol{\Psi} | \boldsymbol{\sigma}_z \otimes \mathbf{1} | \boldsymbol{\Psi} \rangle \\ &= 2 \sum_{i<j,k<l} d_{ij}^* d_{kl} \int d\mathbf{r}\, d\mathbf{r}' \boldsymbol{\Psi}_{ij}^\dagger(\mathbf{r}, \mathbf{r}') \boldsymbol{\sigma}_z \otimes \mathbf{1} \boldsymbol{\Psi}_{kl}(\mathbf{r}, \mathbf{r}'),\end{aligned} \tag{D2}$$

with $\boldsymbol{\sigma}_z \equiv \sigma_z \otimes \mathbf{1}_3$ and the identity matrix $\mathbf{1} \equiv \mathbf{1}_6$. By defining $\sigma_{ijkl} = \langle i|\sigma_z|k\rangle \delta_{jl} + \langle j|\sigma_z|l\rangle \delta_{ik}$, with, for example, $\langle i|\sigma_z|k\rangle = \int d\mathbf{r}\, \boldsymbol{\psi}_i^\dagger(\mathbf{r}) \boldsymbol{\sigma}_z \boldsymbol{\psi}_k(\mathbf{r})$, we can write the formula for the total spin compactly:

$$\langle \sigma_z \rangle = \sum_{i<j,k<l} d_{ij}^* d_{kl} \left\{ \sigma_{ijkl} - \sigma_{ijlk} \right\}. \tag{D3}$$

[1] J. M. Gambetta, J. M. Chow, and M. Steffen, Building logical qubits in a superconducting quantum computing system, Npj Quantum Inf. **3**, 1 (2017), article number: 2.
[2] M. Kjaergaard, M. E. Schwartz, J. Braumüller, P. Krantz, J. I.-J. Wang, S. Gustavsson, and W. D. Oliver, Superconducting qubits: Current state of play, Annu. Rev. Condens. Matter Phys. **11**, 369 (2020).
[3] F. Arute, K. Arya, R. Babbush, D. Bacon, J. C. Bardin, R. Barends, R. Biswas, S. Boixo, F. G. Brandao, and D. A. Buell *et al.*, Quantum supremacy using a programmable superconducting processor, Nature **574**, 505 (2019).
[4] J. Roffe, Quantum error correction: An introductory guide, Contemporary Phys. **60**, 226 (2019).

[5] F. A. Zwanenburg, A. S. Dzurak, A. Morello, M. Y. Simmons, L. C. L. Hollenberg, G. Klimeck, S. Rogge, S. N. Coppersmith, and M. A. Eriksson, Silicon quantum electronics, Rev. Mod. Phys. **85**, 961 (2013).

[6] D. Kim, Z. Shi, C. B. Simmons, D. R. Ward, J. R. Prance, T. S. Koh, J. K. Gamble, D. E. Savage, M. G. Lagally, M. Friesen, S. N. Coppersmith, and M. A. Eriksson, Quantum control and process tomography of a semiconductor quantum dot hybrid qubit, Nature **511**, 70 (2014).

[7] D. M. Zajac, A. J. Sigillito, M. Russ, F. Borjans, J. M. Taylor, G. Burkard, and J. R. Petta, Resonantly driven cnot gate for electron spins, Science **359**, 439 (2018).

[8] T. F. Watson, S. G. J. Philips, E. Kawakami, D. R. Ward, P. Scarlino, M. Veldhorst, D. E. Savage, M. G. Lagally, M. Friesen, S. N. Coppersmith, M. A. Eriksson, and L. M. K. Vandersypen, A programmable two-qubit quantum processor in silicon, Nature **555**, 633 (2018).

[9] X. Mi, M. Benito, S. Putz, D. M. Zajac, J. M. Taylor, G. Burkard, and J. R. Petta, A coherent spin–photon interface in silicon, Nature **555**, 599 (2018).

[10] A. J. Landig, J. V. Koski, P. Scarlino, U. C. Mendes, A. Blais, C. Reichl, W. Wegscheider, A. Wallraff, K. Ensslin, and T. Ihn, Coherent spin–photon coupling using a resonant exchange qubit, Nature **560**, 179 (2018).

[11] G. Zheng, N. Samkharadze, M. L. Noordam, N. Kalhor, D. Brousse, A. Sammak, G. Scappucci, and L. M. K. Vandersypen, Rapid gate-based spin read-out in silicon using an on-chip resonator, Nat. Nanotechnol. **14**, 742 (2019).

[12] L. Petit, H. G. J. Eenink, M. Russ, W. I. L. Lawrie, N. W. Hendrickx, S. G. J. Philips, J. S. Clarke, L. M. K. Vandersypen, and M. Veldhorst, Universal quantum logic in hot silicon qubits, Nature **580**, 355 (2020).

[13] A. Kormányos, V. Zólyomi, N. D. Drummond, and G. Burkard, Spin-Orbit Coupling, Quantum Dots, and Qubits in Monolayer Transition Metal Dichalcogenides, Phys. Rev. X **4**, 011034 (2014).

[14] K. Kośmider, J. W. González, and J. Fernández-Rossier, Large spin splitting in the conduction band of transition metal dichalcogenide monolayers, Phys. Rev. B **88**, 245436 (2013).

[15] G. Y. Wu, N.-Y. Lue, and L. Chang, Graphene quantum dots for valley-based quantum computing: A feasibility study, Phys. Rev. B **84**, 195463 (2011).

[16] Y. Wu, Q. Tong, G.-B. Liu, H. Yu, and W. Yao, Spin-valley qubit in nanostructures of monolayer semiconductors: Optical control and hyperfine interaction, Phys. Rev. B **93**, 045313 (2016).

[17] J. Pawłowski, D. Żebrowski, and S. Bednarek, Valley qubit in a gated MoS_2 monolayer quantum dot, Phys. Rev. B **97**, 155412 (2018).

[18] N. Rohling and G. Burkard, Universal quantum computing with spin and valley states, New J. Phys. **14**, 083008 (2012).

[19] J. Pawłowski, Spin-valley system in a gated MoS_2-monolayer quantum dot, New J. Phys. **21**, 123029 (2019).

[20] K. E. J. Goh, F. Bussolotti, C. S. Lau, D. Kotekar-Patil, Z. E. Ooi, and J. Y. Chee, Toward valley-coupled spin qubits, Adv. Quantum Technol. **3**, 1900123 (2020).

[21] E. A. Laird, F. Pei, and L. P. Kouwenhoven, A valley–spin qubit in a carbon nanotube, Nat. Nanotechnol. **8**, 565 (2013).

[22] F. Pei, E. A. Laird, G. A. Steele, and L. P. Kouwenhoven, Valley–spin blockade and spin resonance in carbon nanotubes, Nat. Nanotechnol. **7**, 630 (2012).

[23] Z. Gong, G.-B. Liu, H. Yu, D. Xiao, X. Cui, X. Xu, and W. Yao, Magnetoelectric effects and valley-controlled spin quantum gates in transition metal dichalcogenide bilayers, Nat. Commun. **4**, 1 (2013), article number: 2053.

[24] C. J. Ciccarino, C. Chakraborty, D. R. Englund, and P. Narang, Carrier dynamics and spin–valley–layer effects in bilayer transition metal dichalcogenides, Faraday Discuss. **214**, 175 (2019).

[25] M. Eich, F. c. v. Herman, R. Pisoni, H. Overweg, A. Kurzmann, Y. Lee, P. Rickhaus, K. Watanabe, T. Taniguchi, M. Sigrist, T. Ihn, and K. Ensslin, Spin and Valley States in Gate-Defined Bilayer Graphene Quantum Dots, Phys. Rev. X **8**, 031023 (2018).

[26] N. E. Penthorn, J. S. Schoenfield, J. D. Rooney, L. F. Edge, and H. Jiang, Two-axis quantum control of a fast valley qubit in silicon, Npj Quantum Inf. **5**, 1 (2019), article number: 94.

[27] X. Mi, S. Kohler, and J. R. Petta, Landau-zener interferometry of valley-orbit states in si/sige double quantum dots, Phys. Rev. B **98**, 161404 (2018).

[28] M. Settnes, S. R. Power, M. Brandbyge, and A.-P. Jauho, Graphene Nanobubbles as Valley Filters and Beam Splitters, Phys. Rev. Lett. **117**, 276801 (2016).

[29] J. R. Schaibley, H. Yu, G. Clark, P. Rivera, J. S. Ross, K. L. Seyler, W. Yao, and X. Xu, Valleytronics in 2d materials, Nat. Rev. Mater. **1**, 1 (2016).

[30] T. Sekera, C. Bruder, E. J. Mele, and R. P. Tiwari, Switchable valley filter based on a graphene $p-n$ junction in a magnetic field, Phys. Rev. B **95**, 205431 (2017).

[31] G. Scuri, T. I. Andersen, Y. Zhou, D. S. Wild, J. Sung, R. J. Gelly, D. Bérubé, H. Heo, L. Shao, A. Y. Joe, A. M. Mier Valdivia, T. Taniguchi, K. Watanabe, M. Lončar, P. Kim, M. D. Lukin, and H. Park, Electrically Tunable Valley Dynamics in Twisted wse_2/wse_2 Bilayers, Phys. Rev. Lett. **124**, 217403 (2020).

[32] D. Xiao, G.-B. Liu, W. Feng, X. Xu, and W. Yao, Coupled Spin and Valley Physics in Monolayers of MoS_2 and Other Group-VI Dichalcogenides, Phys. Rev. Lett. **108**, 196802 (2012).

[33] T. Cao, G. Wang, W. Han, H. Ye, C. Zhu, J. Shi, Q. Niu, P. Tan, E. Wang, B. Liu, and J. Feng, Valley-selective circular dichroism of monolayer molybdenum disulphide, Nat. Commun. **3**, 887 (2012).

[34] K. F. Mak, K. He, J. Shan, and T. F. Heinz, Control of valley polarization in monolayer MoS_2 by optical helicity, Nat. Nanotechnol. **7**, 494 (2012).

[35] H. Zeng, J. Dai, W. Yao, D. Xiao, and X. Cui, Valley polarization in MoS_2 monolayers by optical pumping, Nat. Nanotechnol. **7**, 490 (2012).

[36] G. Wang, A. Chernikov, M. M. Glazov, T. F. Heinz, X. Marie, T. Amand, and B. Urbaszek, Colloquium: Excitons in atomically thin transition metal dichalcogenides, Rev. Mod. Phys. **90**, 021001 (2018).

[37] A. S. Baimuratov and A. Högele, Valley-selective energy transfer between quantum dots in atomically thin semiconductors, Sci. Rep. **10**, 1 (2020).

[38] A. M. Jones, H. Yu, N. J. Ghimire, S. Wu, G. Aivazian, J. S. Ross, B. Zhao, J. Yan, D. G. Mandrus, D. Xiao, W. Yao, and X. Xu, Optical generation of excitonic valley coherence in monolayer WSe2, Nat. Nanotechnol. **8**, 634 (2013).

[39] G. Wang, X. Marie, B. L. Liu, T. Amand, C. Robert, F. Cadiz, P. Renucci, and B. Urbaszek, Control of Exciton Valley Coherence in Transition Metal Dichalcogenide Monolayers, Phys. Rev. Lett. **117**, 187401 (2016).

[40] K. Hao, G. Moody, F. Wu, C. K. Dass, L. Xu, C.-H. Chen, L. Sun, M.-Y. Li, L.-J. Li, A. H. MacDonald, and X. Li, Direct measurement of exciton valley coherence in monolayer WSe2, Nat. Phys. **12**, 677 (2016).

[41] A. Srivastava, M. Sidler, A. V. Allain, D. S. Lembke, A. Kis, and A. Imamoglu, Valley zeeman effect in elementary optical excitations of monolayer WSe2, Nat. Phys. **11**, 141 (2015).

[42] G. Aivazian, Z. Gong, A. M. Jones, R.-L. Chu, J. Yan, D. G. Mandrus, C. Zhang, D. Cobden, W. Yao, and X. Xu, Magnetic control of valley pseudospin in monolayer WSe2, Nat. Phys. **11**, 148 (2015).

[43] T. Scrace, Y. Tsai, B. Barman, L. Schweidenback, A. Petrou, G. Kioseoglou, I. Ozfidan, M. Korkusiński, and P. Hawrylak, Magnetoluminescence and valley polarized state of a two-dimensional electron gas in WS2 monolayers, Nat. Nano **10**, 603 (2015).

[44] J. E. H. Braz, B. Amorim, and E. V. Castro, Valley-polarized magnetic state in hole-doped monolayers of transition-metal dichalcogenides, Phys. Rev. B **98**, 161406 (2018).

[45] D. Miserev, J. Klinovaja, and D. Loss, Exchange intervalley scattering and magnetic phase diagram of transition metal dichalcogenide monolayers, Phys. Rev. B **100**, 014428 (2019).

[46] K. F. Mak, K. He, C. Lee, G. H. Lee, J. Hone, T. F. Heinz, and J. Shan, Tightly bound trions in monolayer MoS_2, Nat. Mater. **12**, 207 (2013).

[47] J. Jadczak, J. Kutrowska-Girzycka, P. Kapuściński, Y. S. Huang, A. Wójs, and L. Bryja, Probing of free and localized excitons and trions in atomically thin WSe2, WS2, $MoSe_2$ and MoS_2 in photoluminescence and reflectivity experiments, Nanotechnology **28**, 395702 (2017).

[48] P. Back, M. Sidler, O. Cotlet, A. Srivastava, N. Takemura, M. Kroner, and A. Imamoğlu, Giant Paramagnetism-Induced Valley Polarization of Electrons in Charge-Tunable Monolayer $MoSe_2$, Phys. Rev. Lett. **118**, 237404 (2017).

[49] J. G. Roch, G. Froehlicher, N. Leisgang, P. Makk, K. Watanabe, T. Taniguchi, and R. J. Warburton, Spin-polarized electrons in monolayer MoS_2, Nat. Nanotechnol. **14**, 432 (2019).

[50] J. Jadczak, L. Bryja, J. Kutrowska-Girzycka, P. Kapuscinski, M. Bieniek, Y.-S. Huang, and P. Hawrylak, Room temperature multi-phonon upconversion photoluminescence in monolayer semiconductor WS_2, Nat. Commun. **10**, 107 (2019).

[51] J. Jadczak, J. J. Kutrowska-Girzycka, M. Bieniek, T. Kazimierczuk, P. Kossacki, J. J. J. Schindler, J. Debus, K. Watanabe, T. Taniguchi, C.-H. Ho, A. Wójs, P. Hawrylak, and L. Bryja, Probing of negatively charged and neutral excitons in MoS_2/hbn and hbn/MoS_2/hbn van der waals heterostructures, Nanotechnology (2020).

[52] K. Wang, K. De Greve, L. A. Jauregui, A. Sushko, A. High, Y. Zhou, G. Scuri, T. Taniguchi, K. Watanabe, M. D. Lukin, H. Park, and P. Kim, Electrical control of charged carriers and excitons in atomically thin materials, Nat. Nanotechnol. **13**, 128 (2018).

[53] M. Brotons-Gisbert, A. Branny, S. Kumar, R. Picard, R. Proux, M. Gray, K. S. Burch, K. Watanabe, T. Taniguchi, and B. D. Gerardot, Coulomb blockade in an atomically thin quantum dot coupled to a tunable fermi reservoir, Nat. Nanotechnol. **14**, 442 (2019).

[54] J. Klinovaja and D. Loss, Spintronics in MoS_2 monolayer quantum wires, Phys. Rev. B **88**, 075404 (2013).

[55] G.-B. Liu, H. Pang, Y. Yao, and W. Yao, Intervalley coupling by quantum dot confinement potentials in monolayer transition metal dichalcogenides, New J. Phys. **16**, 105011 (2014).

[56] S. Pavlović and F. M. Peeters, Electronic properties of triangular and hexagonal MoS_2 quantum dots, Phys. Rev. B **91**, 155410 (2015).

[57] A. C. Dias, J. Fu, L. Villegas-Lelovsky, and F. Qu, Robust effective zeeman energy in monolayer MoS_2 quantum dots, J. Phys.: Condens. Matter **28**, 375803 (2016).

[58] M. Brooks and G. Burkard, Spin-degenerate regimes for single quantum dots in transition metal dichalcogenide monolayers, Phys. Rev. B **95**, 245411 (2017).

[59] F. Qu, A. C. Dias, J. Fu, L. Villegas-Lelovsky, and D. L. Azevedo, Tunable spin and valley dependent magneto-optical absorption in molybdenum disulfide quantum dots, Sci. Rep. **7**, 41044 (2017).

[60] G. Széchenyi, L. Chirolli, and A. Pályi, Impurity-assisted electric control of spin-valley qubits in monolayer MoS_2, 2D Materials **5**, 035004 (2018).

[61] A. David, G. Burkard, and A. Kormányos, Effective theory of monolayer TMDC double quantum dots, 2D Materials **5**, 035031 (2018).

[62] Q. Chen, L. L. Li, and F. M. Peeters, Magnetic field dependence of electronic properties of MoS_2 quantum dots with different edges, Phys. Rev. B **97**, 085437 (2018).

[63] F.-W. Chen and Y.-S. G. Wu, Theory of field-modulated spin valley orbital pseudospin physics, Phys. Rev. Res. **2**, 013076 (2020).

[64] M. Brooks and G. Burkard, Electric dipole spin resonance of two-dimensional semiconductor spin qubits, Phys. Rev. B **101**, 035204 (2020).

[65] X.-X. Song, D. Liu, V. Mosallanejad, J. You, T.-Y. Han, D.-T. Chen, H.-O. Li, G. Cao, M. Xiao, G.-C. Guo, and G.-P. Guo, A gate defined quantum dot on the two-dimensional transition metal dichalcogenide semiconductor WSe_2, Nanoscale **7**, 16867 (2015).

[66] Z.-Z. Zhang, X.-X. Song, G. Luo, G.-W. Deng, V. Mosallanejad, T. Taniguchi, K. Watanabe, H.-O. Li, G. Cao, G.-C. Guo, F. Nori, and G.-P. Guo, Electrotunable artificial molecules based on van der waals heterostructures, Sci. Adv. **3**, e1701699 (2017).

[67] R. Pisoni, A. Kormányos, M. Brooks, Z. Lei, P. Back, M. Eich, H. Overweg, Y. Lee, P. Rickhaus, K. Watanabe, T. Taniguchi, A. Imamoglu, G. Burkard, T. Ihn, and

K. Ensslin, Interactions and Magnetotransport through Spin-Valley Coupled Landau Levels in Monolayer MoS_2, Phys. Rev. Lett. **121**, 247701 (2018).

[68] C. S. Lau, J. Y. Chee, D. Thian, H. Kawai, J. Deng, S. L. Wong, Z. E. Ooi, Y.-F. Lim, and K. E. J. Goh, Carrier control in 2D transition metal dichalcogenides with Al2O3 dielectric, Sci. Rep. **9**, 8769 (2019).

[69] S. Davari, J. Stacy, A. Mercado, J. Tull, R. Basnet, K. Pandey, K. Watanabe, T. Taniguchi, J. Hu, and H. Churchill, Gate-Defined Accumulation-Mode Quantum Dots in Monolayer and Bilayer WSe_2, Phys. Rev. Appl. **13**, 054058 (2020).

[70] K. E. J. Goh, F. Bussolotti, C. S. Lau, D. Kotekar-Patil, Z. E. Ooi, and J. Y. Chee, Toward valley-coupled spin qubits, Adv. Quantum Technol. **3**, 1900123 (2020).

[71] L. Chirolli, E. Prada, F. Guinea, R. Roldán, and P. San-Jose, Strain-induced bound states in transition-metal dichalcogenide bubbles, 2D Materials **6**, 025010 (2019).

[72] M. Bieniek, L. Szulakowska, and P. Hawrylak, Effect of valley, spin, and band nesting on the electronic properties of gated quantum dots in a single layer of transition metal dichalcogenides, Phys. Rev. B **101**, 035401 (2020).

[73] L. Szulakowska, M. Cygorek, M. Bieniek, and P. Hawrylak, Valley- and spin-polarized broken-symmetry states of interacting electrons in gated MoS_2 quantum dots, Phys. Rev. B **102**, 245410 (2020).

[74] M. Ciorga, A. S. Sachrajda, P. Hawrylak, C. Gould, P. Zawadzki, S. Jullian, Y. Feng, and Z. Wasilewski, Addition spectrum of a lateral dot from coulomb and spin-blockade spectroscopy, Phys. Rev. B **61**, R16315 (2000).

[75] M. Bayer, P. Hawrylak, K. Hinzer, S. Fafard, M. Korkusinski, Z. Wasilewski, O. Stern, and A. Forchel, Coupling and entangling of quantum states in quantum dot molecules, Science **291**, 451 (2001).

[76] M. Pioro-Ladrière, M. Ciorga, J. Lapointe, P. Zawadzki, M. Korkusiński, P. Hawrylak, and A. S. Sachrajda, Spin-Blockade Spectroscopy of a Two-Level Artificial Molecule, Phys. Rev. Lett. **91**, 026803 (2003).

[77] M. Pioro-Ladrière, M. R. Abolfath, P. Zawadzki, J. Lapointe, S. A. Studenikin, A. S. Sachrajda, and P. Hawrylak, Charge sensing of an artificial h_2^+ molecule in lateral quantum dots, Phys. Rev. B **72**, 125307 (2005).

[78] W. Dybalski and P. Hawrylak, Two electrons in a strongly coupled double quantum dot: From an artificial helium atom to a hydrogen molecule, Phys. Rev. B **72**, 205432 (2005).

[79] T. Pei, A. Pályi, M. Mergenthaler, N. Ares, A. Mavalankar, J. H. Warner, G. A. D. Briggs, and E. A. Laird, Hyperfine and Spin-Orbit Coupling Effects on Decay of Spin-Valley States in a Carbon Nanotube, Phys. Rev. Lett. **118**, 177701 (2017).

[80] A. Laturia, M. L. Van de Put, and W. G. Vandenberghe, Dielectric properties of hexagonal boron nitride and transition metal dichalcogenides: From monolayer to bulk, Npj 2D Materials Appl. **2**, 6 (2018).

[81] J. Pawłowski, P. Szumniak, and S. Bednarek, Electron spin rotations induced by oscillating rashba interaction in a quantum wire, Phys. Rev. B **93**, 045309 (2016).

[82] M. Bieniek, M. Korkusiński, L. Szulakowska, P. Potasz, I. Ozfidan, and P. Hawrylak, Band nesting, massive dirac fermions, and valley landé and zeeman effects in transition metal dichalcogenides: A tight-binding model, Phys. Rev. B **97**, 085153 (2018).

[83] H. Rostami, A. G. Moghaddam, and R. Asgari, Effective lattice hamiltonian for monolayer MoS_2: Tailoring electronic structure with perpendicular electric and magnetic fields, Phys. Rev. B **88**, 085440 (2013).

[84] E. Ridolfi, D. Le, T. S. Rahman, E. R. Mucciolo, and C. H. Lewenkopf, A tight-binding model for MoS_2 monolayers, J. Phys.: Condens. Matter **27**, 365501 (2015).

[85] G.-B. Liu, W.-Y. Shan, Y. Yao, W. Yao, and D. Xiao, Te-band tight-binding model for monolayers of group-vib transition metal dichalcogenides, Phys. Rev. B **88**, 085433 (2013).

[86] E. S. Kadantsev and P. Hawrylak, Electronic structure of a single MoS_2 monolayer, Solid State Commun. **152**, 909 (2012).

[87] D. P. Żebrowski, F. M. Peeters, and B. Szafran, Double quantum dots defined in bilayer graphene, Phys. Rev. B **96**, 035434 (2017).

[88] B. Szafran and D. Żebrowski, Spin and valley control in single and double electrostatic silicene quantum dots, Phys. Rev. B **98**, 155305 (2018).

[89] E. N. Osika and B. Szafran, Two-electron $n-p$ double quantum dots in carbon nanotubes, Phys. Rev. B **91**, 085312 (2015).

[90] E. N. Osika, A. Chacón, M. Lewenstein, and B. Szafran, Spin-valley dynamics of electrically driven ambipolar carbon-nanotube quantum dots, J. Phys.: Condens. Matter **29**, 285301 (2017).

[91] P. Potasz, A. D. Güçlü, and P. Hawrylak, Spin and electronic correlations in gated graphene quantum rings, Phys. Rev. B **82**, 075425 (2010).

[92] A. D. Güçlü, P. Potasz, O. Voznyy, M. Korkusinski, and P. Hawrylak, Magnetism and Correlations in Fractionally Filled Degenerate Shells of Graphene Quantum Dots, Phys. Rev. Lett. **103**, 246805 (2009).

[93] P. Potasz, A. D. Güçlü, A. Wójs, and P. Hawrylak, Electronic properties of gated triangular graphene quantum dots: Magnetism, correlations, and geometrical effects, Phys. Rev. B **85**, 075431 (2012).

[94] G. P. Lepage, A new algorithm for adaptive multidimensional integration, J. Comput. Phys. **27**, 192 (1978).

[95] J. C. Slater, Atomic shielding constants, Phys. Rev. **36**, 57 (1930).

[96] M. Lesiuk and R. Moszynski, Reexamination of the calculation of two-center, two-electron integrals over slater-type orbitals. i. coulomb and hybrid integrals, Phys. Rev. E **90**, 063318 (2014).

[97] E. Clementi, D. L. Raimondi, and W. P. Reinhardt, Atomic screening constants from scf functions. ii. atoms with 37 to 86 electrons, J. Chem. Phys. **47**, 1300 (1967).

[98] G. Kresse and D. Joubert, From ultrasoft pseudopotentials to the projector augmented-wave method, Phys. Rev. B **59**, 1758 (1999).

[99] J. P. Perdew, K. Burke, and M. Ernzerhof, Generalized Gradient Approximation Made Simple, Phys. Rev. Lett. **77**, 3865 (1996).

[100] G. Kresse and J. Furthmüller, Efficient iterative schemes for ab initio total-energy calculations using a plane-wave basis set, Phys. Rev. B **54**, 11169 (1996).

[101] D. R. Hofstadter, Energy levels and wave functions of bloch electrons in rational and irrational magnetic fields, Phys. Rev. B **14**, 2239 (1976).

[102] A. Barenco, C. H. Bennett, R. Cleve, D. P. DiVincenzo, N. Margolus, P. Shor, T. Sleator, J. A. Smolin, and H. Weinfurter, Elementary gates for quantum computation, Phys. Rev. A **52**, 3457 (1995).

[103] H. Fan, V. Roychowdhury, and T. Szkopek, Optimal two-qubit quantum circuits using exchange interactions, Phys. Rev. A **72**, 052323 (2005).

[104] K. Nowack, M. Shafiei, M. Laforest, G. Prawiroatmodjo, L. Schreiber, C. Reichl, W. Wegscheider, and L. Vandersypen, Single-shot correlations and two-qubit gate of solid-state spins, Science **333**, 1269 (2011).

[105] R. Hanson, L. P. Kouwenhoven, J. R. Petta, S. Tarucha, and L. M. K. Vandersypen, Spins in few-electron quantum dots, Rev. Mod. Phys. **79**, 1217 (2007).

[106] A. Pályi and G. Burkard, Spin-valley blockade in carbon nanotube double quantum dots, Phys. Rev. B **82**, 155424 (2010).

[107] J. K. Perron, M. D. Stewart, and N. M. Zimmerman, A new regime of pauli-spin blockade, J. Appl. Phys. **119**, 134307 (2016).

[108] E. J. Santos and E. Kaxiras, Electric-field dependence of the effective dielectric constant in graphene, Nano Lett. **13**, 898 (2013).

[109] R. Geick, C. H. Perry, and G. Rupprecht, Normal modes in hexagonal boron nitride, Phys. Rev. **146**, 543 (1966).

[110] L. Keldysh, Coulomb interaction in thin semiconductor and semimetal films, JETP Lett **29**, 658 (1979).

[111] S. Schmitt-Rink and C. Ell, in *High Excitation and Short Pulse Phenomena*, edited by M. Pilkuhn (Elsevier, Amsterdam, 1985), p. 585.

[112] D. Van Tuan, M. Yang, and H. Dery, Coulomb interaction in monolayer transition-metal dichalcogenides, Phys. Rev. B **98**, 125308 (2018).

[113] T. C. Berkelbach and D. R. Reichman, Optical and excitonic properties of atomically thin transition-metal dichalcogenides, Annu. Rev. Condens. Matter Phys. **9**, 379 (2018).

[114] P. Cudazzo, I. V. Tokatly, and A. Rubio, Dielectric screening in two-dimensional insulators: Implications for excitonic and impurity states in graphane, Phys. Rev. B **84**, 085406 (2011).